A CDK-mediated phosphorylation switch of disordered protein condensation

Authors: Juan Manuel Valverde[1,2†], Geronimo Dubra[3,4†], Henk van den Toorn[1,2], Austin Haider[8], Michael Phillips[8], Albert J.R. Heck[1,2], Carlos Elena-Real[5], Aurélie Fournet[5], Emile Al Ghoul[7], Dhanvantri Chahar[3,4], Nuria Andrés-Sanchez[3,4], Matteo Paloni[5], Guido van Mierlo[6], Michiel Vermeulen[6], Angelos Constantinou[7], Alessandro Barducci[5], Kingshuk Ghosh[8], Pau Bernado[5], Nathalie Sibille[5], Puck Knipscheer[9], Liliana Krasinska[3,4‡], Daniel Fisher[3,4‡*], Maarten Altelaar[1,2‡*]

Affiliations:

[1]Biomolecular Mass Spectrometry and Proteomics, Bijvoet Center for Biomolecular Research and Utrecht Institute for Pharmaceutical Sciences, University of Utrecht, Utrecht, 3584 CH Utrecht, Netherlands.

[2]Netherlands Proteomics Center, Padualaan 8, 3584 CH Utrecht, Netherlands.

[3]IGMM, University of Montpellier, CNRS, Inserm, Montpellier, France.

[4]Equipe Labellisée LIGUE 2018, Ligue Nationale Contre le Cancer, Paris, France.

[5]CBS, University of Montpellier, INSERM, CNRS, Montpellier, France.

[6]Department of Molecular Biology, Faculty of Science, Radboud Institute for Molecular Life Sciences, Oncode Institute, Radboud University Nijmegen, 6525 GA Nijmegen, the Netherlands.

[7]IGH, University of Montpellier, CNRS, Montpellier, France.

[8] Department of Physics and Astronomy, and Department of Molecular and Cellular Biophysics, University of Denver, Denver, Colorado 80208, USA.

[9]Oncode Institute, Hubrecht Institute–KNAW and University Medical Center, Utrecht, 3584 CT, Netherlands.

*Correspondence to: m.altelaar@uu.nl and daniel.fisher@igmm.cnrs.fr

†‡ Equal contributions

Cell cycle transitions result from global changes in protein phosphorylation states triggered by cyclin-dependent kinases (CDKs). To understand how this complexity produces an ordered

and rapid cellular reorganisation, we generated a high-resolution map of changing phosphosites throughout unperturbed early cell cycles in single *Xenopus* embryos, derived the emergent principles through systems biology analysis, and tested them by biophysical modelling and biochemical experiments. We found that most dynamic phosphosites share two key characteristics: they occur on highly disordered proteins that localise to membraneless organelles, and are CDK targets. Furthermore, CDK-mediated multisite phosphorylation can switch homotypic interactions of such proteins between favourable and inhibitory modes for biomolecular condensate formation. These results provide insight into the molecular mechanisms and kinetics of mitotic cellular reorganisation.

Introduction

The cell cycle is driven by CDKs, which are essential to promote entry into S-phase and mitosis. Two general strategies have been used to understand how CDK-dependent phosphorylation brings about these transitions[1]. First, top-down screens have revealed key system components. Hundreds of CDK substrates [2–7] and cell cycle-regulated proteins [8] and thousands of mitotic phosphorylations [9] have been identified in this manner. Yet determining their roles has lagged behind; for example, painstaking genetic analysis in yeast models was required to reveal the requirement for CDK-mediated phosphorylation of two key substrates to allow DNA replication[10,11]. Second, bottom-up molecular analysis of the structural effects of individual phosphorylations on single proteins provides mechanistic insight into regulation of their activity [12]. Both of these approaches are rendered more difficult by the fact that CDKs often phosphorylate multiple sites, whose combined effects may result in a phenotype; for example, multisite phosphorylation of the CDK inhibitor Sic1 in budding yeast is required to prevent its degradation [13]. As such, it has proven challenging to use studies performed from these different perspectives to understand global cellular behaviour.

Different models of CDK-mediated phosphorylation have been proposed. Specific interactions between distinct CDK-cyclin complexes and sequence motifs encoded in substrates might result in highly ordered phosphorylation [14], yet such complex mechanisms may not be essential since the cell cycle can be driven by single CDK1-cyclin complexes [15,16]. Furthermore, theoretical modelling and biochemical analysis have suggested that the mitotic control network can trigger switch-like activation of CDK1 [17], yet approaches using fluorescent biosensors imply that mitotic CDK1 activation is rather progressive [18]. Along with the CDK-mediated ordered phosphorylation model, this suggests that mitotic phosphorylation states should change progressively *in vivo*, yet mitotic reorganisation is rapid and abrupt. Thus, understanding cell

cycle transitions requires a description of the dynamics of global mitotic phosphorylation, which is largely unknown, as well as an investigation of the biochemical effects of phosphorylations, most of which remain uncharacterised. We reasoned that this would require a multidisciplinary quantitative approach involving cell biology, biochemistry, bioinformatics and biophysics. We aimed to generate a quantitative time-resolved map of *in vivo* cell cycle phosphorylation, extract global principles of phosphorylation dynamics, perform comparative analysis to assess conservation of these principles across species, and analyse effects of phosphorylation by modelling, biophysical approaches and biochemical experiments.

Results

A high-resolution map of in vivo cell cycle phosphorylation

Dynamic phosphorylation states cannot be determined from cell populations [19], while single-cell proteomics studies [20,21] currently have insufficient sensitivity and reproducibility for low stoichiometry and dynamic targets. We wanted to identify and quantify cell cycle-regulated phosphosites in a system devoid of artifacts arising from cell synchronisation [22,23], and with temporal resolution that alternative approaches, like centrifugal elutriation [24] or FACS [25] cannot provide. We thus took advantage of the naturally synchronous early cell cycles of *Xenopus laevis* embryos [26,27]. We performed quantitative phosphoproteomics *in vivo* using a sensitive phosphopeptide enrichment strategy [28]. We collected single embryos at 15-minute intervals while recording visual cues of cell divisions, and phosphopeptides from each embryo were purified and analysed by mass spectrometry (Fig. 1a). These individual embryo phosphorylation states strongly correlated (Supplementary Fig. 1a). We identified 4583 high-confidence phosphosites mapping to 1843 proteins (Supplementary Fig. 1b; Supplementary Dataset 1), most being phosphoserines (Supplementary Fig. 1c). Our approach thus allowed us to generate a dynamic map of protein phosphorylation from an unfertilised egg to a 16-cell embryo.

We focused on 1032 sites on 646 proteins whose phosphorylation state changed over time (hereafter denoted “dynamic phosphosites”). Gene ontology (GO) and network analysis of proteins harbouring these sites revealed high functional association and interconnectivity between groups of proteins involved in RNA binding and the nuclear pore complex (NPC), DNA replication and chromatin remodeling, and microtubule regulation (Fig. 1b). Hierarchical clustering uncovered four groups with distinct dynamic behaviour (Fig. 1c; Supplementary

Dataset 1). The levels of clusters A and B phosphosites were highest in eggs and post-fertilisation, and decreased during the first round of DNA replication. GO analysis for group A highlighted proteins involved in RNA regulation and nuclear organisation, including the NPC and nuclear transport, chromosomal structure and segregation (Supplementary Fig. 1d), as also observed in a recent study on meiosis exit [29]. Cluster B phosphosites were enriched in regulators of RNA biosynthesis and stability, translation, actin, DNA replication and repair (Supplementary Fig. 1d). Dephosphorylation of these sites, which coincide with the meiosis-zygote transition, may prepare the embryo for upcoming cell divisions [30]. Cluster C phosphosites progressively increased after meiotic exit, while cluster D phosphosites had a clear oscillating signature with upregulation preceding each cell division. GO analysis of cluster C showed dominance of interphase cell cycle processes including DNA replication, RNA-related processes and chromosome organisation (Supplementary Fig. 1d). Several sites were from monophosphorylated peptides, while the multiphosphorylated forms were found in clusters A or D (Supplementary Fig. 1e), further indicating that cluster C sites are from interphase. Cluster D shows coordinated phosphorylation of multiple members of protein complexes involved in distinct processes such as nuclear transport, RNA processing, chromatin remodelling and DNA replication, suggesting a common mechanism of regulation (Supplementary Fig. 1f). Importantly, phosphoproteome changes were not simply a reflection of changes in abundance of the corresponding proteins (Supplementary Fig. 2), which are generally negligible during *Xenopus* early development [31]. Together, these results suggest that multisite phosphorylation, rather than progressive phosphorylation, might constitute the mitotic trigger.

To investigate this idea further, we assigned *in vivo* embryo phosphosites to different cell cycle stages by comparing with phosphorylation patterns of replicating or mitotic egg extracts (Fig. 1d). Replication was initiated by adding purified sperm chromatin to interphase egg extracts and quantified over time by measuring radioactive nucleotide incorporation (Fig. 1e, top), while mitosis was triggered by adding recombinant cyclin B and verified microscopically. To compare meiotic exit with mitosis, we also used egg extracts arrested at meiotic metaphase II (Cytostatic Factor, CSF-arrested). Overall, we identified 6937 phosphosites, which included 71% of the sites identified *in vivo* (Fig. 1f, Supplementary Dataset 1). 1728 sites varied between S and M-phase, including 693 sites upregulated in S-phase and 1035 in mitosis (Fig. 1e, Supplementary Dataset 1). The S-phase specific phosphosites detected in this dataset greatly increase the known repertoire of phosphorylation sites upregulated during DNA replication [9].

Although several DNA-replication factors, including MCM4 and RIF1, were already phosphorylated in S-phase, they displayed marked multi-site phosphorylation in mitosis (Supplementary Fig. 3a). GO analysis of interphase and mitotic sites revealed processes enriched in *in vivo* cluster C and cluster D, respectively (Supplementary Fig. 3b).

We next analysed the cell cycle behaviour of the dynamic phosphosites that we identified *in vivo* (Supplementary Fig. 3c). Most embryo cluster A sites were upregulated in both CSF-arrested meiotic extracts and mitotic extracts, highlighting the global similarities of meiotic and mitotic M-phase, despite the additional activity of the Mos/MEK/MAP kinase pathway in meiosis. In contrast, 78% of embryo cluster B sites were not mapped in extracts, suggesting that these are specific to the developmental transition from meiosis to early embryogenesis. In agreement, cluster B sites that mapped to extracts were generally low in mitosis. Most sites that mapped from embryo cluster C were present only in S-phase, whereas a subfraction peaked in mitosis. As such, this analysis revealed that clusters B and C do not strictly identify cell cycle phases. In contrast, all mapped cluster D sites were absent in S-phase and high in M-phase *in vitro*, showing that single embryo data can successfully identify mitotic phosphorylations. Next, we assessed the behaviour of the 102 peptides detected in both singly and multi-phosphorylated forms in extracts, and found that they segregated into two distinct clusters corresponding to interphase and M-phase, with a strong enrichment for multisite phosphorylation in M-phase (odds ratio 4.6, adjusted p-value $< 10^{-6}$) (supplementary Fig. 3d). The same analysis of multi-site phosphorylation on the 35 peptides detected in singly or multiply phosphorylated forms in embryos revealed four clusters, which correspond to clusters A-D (supplementary Fig. 3e). Despite the small sample, multi-site phosphorylation was highly enriched in meiotic metaphase cluster A (odds ratio 5.6, adjusted p-value 0.011), while two peptides were present as singly phosphorylated in interphase cluster C and doubly phosphorylated in mitotic cluster D. Overall, these data show that diverse biological processes may share a common regulatory mechanism of multisite phosphorylation during cell cycle progression.

Predominance of CDK targets

We further investigated our detected phosphosites to identify putative kinases responsible for their dynamic phosphorylation. Analysis of kinase consensus motifs showed that proline-directed (**S/T**-P) sites, which conform to the minimal consensus for CDKs, constitute 51% of all detected phosphosites *in vivo* and 60% of dynamic sites (Supplementary Fig. 4a). Around 10% of all phosphosites matched the full CDK1-family consensus motif (**S/T**PxK/R).

Replicating and mitotic extracts displayed a similar trend (Supplementary Fig. 4a). Putative CDK targets dominated all clusters, with 80% of sites in cluster D *in vivo* and mitotic clusters *in vitro* conforming to the minimal CDK motif (Fig.1g, Supplementary Fig. 4b, c). Consensus sites of other kinases such as Aurora, Polo-like kinase (PLK), DBF4-dependent kinase (DDK) and Casein kinase I and II were present to a lesser extent (Supplementary Fig. 4b, d). The fraction of **S/T**-P sites that correspond to the full CDK consensus site motif is lower in clusters A (6%) and B (11%) than in clusters C and D (26 and 21%, respectively). Many of the cluster B **S/T**-P sites are likely mediated by MAP kinases, which are proline-directed kinases that are active in meiotic M-phase but are inactivated during early embryonic cell cycles [32]. In agreement with this idea, the MAP kinase consensus motif (GPL**S**P)[33] is clearly detectable in cluster B (Supplementary Fig. 4c). In contrast, around half of cluster A sites mapped to extracts are present in mitosis; this cluster has an unusual **S**/**T**-P motif that may correspond to a new class of CDK sites phosphorylated with distinct kinetics from cluster D sites.

Few direct CDK substrates have been characterised in *Xenopus*, but we surmised that CDK sites are likely conserved between vertebrates. Thus, to further analyse the proportion of dynamic sites dependent on CDKs, we manually curated a set of 654 human CDK1-subfamily targets (Supplementary Dataset 2; see Supplementary Methods for sources). 304 of these have *Xenopus* homologues among the 1843 phosphoproteins we detected, and 149 were present among the 646 proteins with dynamic phosphosites in *Xenopus* embryos (Fig. 1h). Thus, the predominance of CDK motifs among dynamic phosphosites reflects a high proportion of *bona fide* CDK substrates. This is a conservative estimate, since we only considered proline-directed sites as CDK motifs, although we found that 10-20% of human and yeast CDK substrates (Supplementary Dataset 2; see Supplementary Methods for sources) were non-proline-directed (Supplementary Fig. 4e), confirming a recent finding [34]. These data reinforce the dominant role of CDKs in cell cycle-regulated phosphorylation.

Mechanisms generating synchronous mitotic phosphorylation in vivo

Since contrasting models of CDK activity predict either switch-like or progressive dynamics of substrate phosphorylation, we determined the *in vivo* dynamics of mitotic phosphorylation of individual phosphosites at extremely high-time resolution. We focused on 64 cluster D sites from diverse proteins, 60 of which conform to CDK minimal consensus motifs. We analysed these sites in single embryos every 180-seconds using quantitative targeted phosphoproteomics [35–37] by parallel reaction monitoring [38] (Fig. 2a), and thus obtained a highly resolved quantitative description of mitotic phosphorylation of different protein complexes *in vivo*. This

194 revealed an exceptionally synchronous transition from low to maximal phosphorylation of all
195 phosphosites preceding each cell division (Fig. 2b, c). The latter is as close to switch-like
196 behaviour (an all-or-nothing response to a small change in regulator activity) as can be
197 expected given the spatial metachronicity of mitotic entry in early *Xenopus* embryos [39,40].
198 Therefore, any differences in affinities of CDKs for substrates *in vitro* [14] do not translate into
199 major timing differences in mitotic phosphorylation *in vivo*.

200 Highly synchronous mitotic phosphorylation of diverse proteins did not require oscillation of
201 CDK1-Y15 inhibitory phosphorylation, which was downregulated over time (Fig. 2d), as
202 previously reported [41], consistent with lack of oscillating phosphorylation of the CDK1-Y15-
203 regulatory enzymes, CDC25 and WEE1 (Fig. 2e). In contrast, oscillating phosphorylations on
204 NIPA and the APC/C, which regulate mitotic cyclin accumulation, as well as Greatwall kinase,
205 which activates the PP2A inhibitors Arpp19/ENSA, were apparent (Fig. 2f). This suggests that,
206 in early embryos, control of mitotic cyclin levels and PP2A activity, and thus the overall
207 CDK/phosphatase activity ratio [17], may be the key determinant of substrate phosphorylation
208 timing and generate synchronous mitotic phosphorylation, whereas regulated CDK1-Y15
209 phosphorylation is not essential (Fig. 2g). This is consistent with the self-sufficiency of futile
210 cycles in generating switch-like network output in the absence of allosteric regulation [42], and
211 suggests that multiple layers of regulation may have evolved to ensure robustness of the
212 dynamics.

213 *The cell cycle phosphoproteome is intrinsically disordered*

214 We next investigated whether the diverse dynamic phosphoproteins that we identified share
215 common structural features facilitating CDK-mediated phosphorylation, and if so, whether this
216 is conserved across species. Phosphosites in general are often located in intrinsically disordered
217 regions (IDRs) of proteins [43], which is also true for yeast and mouse CDK sites [44,6,7]. However,
218 previous analyses did not take into account the enrichment of serine, threonine and proline in
219 disordered regions, which is consistently predicted across the entire proteome of *Xenopus*,
220 human and yeast (Supplementary Fig. 5a). Therefore, to date, it is not clear whether the
221 presence of phosphorylatable amino acids, or specifically their phosphorylation, is enriched in
222 disordered regions. We corrected for this compositional bias (see Methods), and found that
223 phosphorylatable residues in IDRs were more highly phosphorylated than those in ordered
224 regions (Fig. 3a-c). This enrichment was increased for proteins with at least one site displaying
225 dynamic phosphorylation; the same was true for human CDK substrates (Fig. 3b, c). To
226 estimate the differential phosphorylation of disordered sites globally, we calculated the ratio of

dynamically phosphorylated (*Xenopus*) or CDK-phosphorylated (yeast, human) to non-phosphorylated serine and threonine in both disordered and structured regions (Supplementary Fig. 5b; see Methods). This showed that cell cycle and CDK-regulated phosphorylation is highly skewed towards disordered regions (Fig. 3d, Supplementary Fig. 5c). We then asked whether this is also true for substrates of other protein kinases, again taking into account compositional bias. We analysed the mitotic PLK and Aurora kinases (which control various aspects of mitotic chromosome and spindle dynamics), DYRK kinases, (which promote mitotic phosphorylation of several intrinsically disordered proteins [IDPs]) [45], NEK kinases (which have roles in centrosome duplication and various stages of mitosis), and MAP kinases (which share the proline-directed S/T minimal consensus site with CDKs). For each of these, with the exception of NEK kinase targets, documented phosphosites were strongly enriched in IDRs (Supplementary Fig. 5c, d), supporting the idea that phosphorylation of residues in IDRs is a general cellular control mechanism and is not specific to CDKs.

Given the preponderance of CDK substrates among cell cycle-regulated phosphosites despite the evidence that many kinases may preferentially phosphorylate IDRs, we wondered whether CDK substrates might be more disordered than phosphoproteins in general. We therefore determined the percentage of disordered residues of proteins in our datasets, compared to the rest of their respective phosphoproteomes (Supplementary Dataset 3). This revealed that, on average, both *Xenopus* dynamic phosphoproteins and human and yeast CDK substrates contain approximately twice the proportion of disordered amino acids as all other phosphoproteins (Fig. 3e, Supplementary Fig. 5e), putting them among the top quartile of proteins with the most disorder in the proteome. Furthermore, targets of most cell cycle kinases except NEK are significantly more disordered than targets of MAP kinase (Fig. 3f), whose phosphosites are also proline-directed and preferentially located in IDRs (Supplementary Fig. 5d). This suggests that several cell cycle kinases have evolved to phosphorylate some of the most disordered proteins in the proteome.

Enrichment of MLO components among CDK substrates

We surmised that the critical importance of intrinsic disorder might underlie a common mechanism of phosphoregulation of diverse proteins during the cell cycle. We noted that IDPs are key components of membrane-less organelles (MLO), many of which (*e.g.* Cajal bodies, nucleoli, nuclear pore complexes, splicing speckles) show cell cycle-regulated assembly or disassembly and are thought to arise by phase separation (PS) [46] that can be controlled by phosphorylation [45,47–49]. We thus hypothesised that CDKs might regulate PS during the cell

cycle. We analysed available data on cellular localisation for each of our curated human CDK substrates, and found that 257 (39.2%) are present in MLOs (Fig. 4a). We then manually curated an MLO proteome from human proteomics studies and asked whether proteins undergoing cell cycle-regulated phosphorylation are enriched in these compartments (Supplementary Dataset 4; See Supplementary Methods for sources). Indeed, homologues of 204 dynamic *Xenopus* phosphoproteins (31.6%) localise to MLOs, as do 73 of the 149 proteins (50%) that show dynamic phosphorylation in *Xenopus* and are CDK substrates in human (Fig. 4a). Of the latter, we studied the location of phosphosites on key IDPs of different MLOs, including coilin (Cajal bodies), nucleophosmin, nucleolin and Ki-67 (nucleoli), 53BP1 (53BP1 bodies), nucleoporins (NPC) and PML (PML bodies). As we anticipated, the vast majority of both proline-directed phosphosites and confirmed CDK sites on these proteins were located in predicted IDRs (Fig. 4b). We next investigated whether dynamically phosphorylated IDPs have properties characteristic of phase separation. We first applied a machine learning classifier [50] to predict whether cell cycle-regulated phosphoproteins show higher propensity to phase separate (PSAP score). Indeed, we observed a sharp increase in the PSAP score, from the proteome to the phosphoproteome, and a further increase for dynamic phosphoproteins, with the highest score for mitotic cluster D (Supplementary Fig. 6). Similarly, the PSAP score is far higher amongst targets of most cell cycle kinases (CDK, Aurora, PLK, but not NEK) and DYRK kinases than the overall phosphoproteome, but less so for MAP kinase substrates.

CDKs regulate IDR phase separation

Both stochastic and specific interactions between IDPs contribute to PS and MLO assembly [46,51,52], and protein phosphorylation can promote or inhibit PS, depending on the protein sequence context [49,53]. Although most MLOs disassemble in mitosis, there is a notable exception: the perichromosomal layer (PCL), which has been hypothesised to form via PS. We reasoned that the degree of CDK-mediated multisite IDP phosphorylation might constitute a switch between PS promotion and inhibition. For example, the maximal CDK activity present at the onset of mitosis might promote both disassembly of most MLOs and formation of the PCL. Studying the effects of CDK-mediated phosphorylation in a considerable number of diverse proteins is not feasible by biochemical approaches and is challenging even for molecular dynamics simulations. To overcome this obstacle, we employed analytical modeling. We took advantage of a newly developed mathematical theory called renormalised Gaussian random phase approximation (rG-RPA) [54], that combines traditional RPA theory with sequence-dependent single-chain theory using a renormalised Gaussian (rG) chain formulation.

This theory provides a better account of conformational heterogeneity and density fluctuations, allows predictions of phase separation, and can be employed at a medium-throughput scale. We supported our findings by another recent theory that computes sequence charge decoration matrices (SCDM) to study conformational properties of a single IDP chain; this accounts for the effects of sequence-specific electrostatic interactions on chain conformation, which dictate the distance between any two amino acid residues [55–57]. Since single chain properties can predict multi-chain physical behaviour, we expect SCDM to provide further insights into the propensity of phase separation. We chose 12 IDPs representing different biological processes and MLOs and containing multiple CDK phosphorylation sites (Supplementary Dataset 5). Phosphorylation of all described CDK-sites lowered critical temperature and phase separation propensity of 8 IDPs (NCL, NPM1, NUP53, ELYS, 53BP1, MCM4, MDC1, and SF3B1) (Fig. 5a). These trends are consistent with SCDM maps showing decreased self-association propensity (increased red regions, Fig. 5b). Conversely, for Ki-67, SRRM2, TICRR and coilin, CDK-mediated phosphorylation increased critical temperature and PS tendency (Fig. 5a), consistent with SCDM maps (increased blue or reduced red regions, Fig. 5b). Overall, these data are in agreement with our hypothesis that CDK-mediated phosphorylation is a key regulator of PS propensity of IDPs.

To analyse this in more detail, we focused on a model CDK substrate, Ki-67, an IDP that organises heterochromatin structure [58] and perichromosomal layer formation from nucleolar components in mitosis [59,60]. Ki-67 is highly phosphorylated in mitosis by CDKs, which regulates its perichromosomal localisation [61]. It contains a multivalent repeat domain of 122 amino acids, known as the Ki-67 repeat, each harbouring a highly conserved motif, the Ki-67 motif, currently of unknown function (Fig. 6a).

To evaluate the possibility that Ki-67 may show PS behaviour in living cells, we expressed a GFP-tagged full length Ki-67 protein and compared its localisation pattern in cells with different expression levels (Fig. 6b). At lower levels, Ki-67 was detectable in the nucleolus, the site of endogenous Ki-67, but not in the nucleoplasm, while at higher levels, additional foci appeared outside the nucleolus. This suggests that Ki-67 is partitioned by PS into dense and dilute phases. At the highest levels, Ki-67 showed a virtually continuous condensed phase, reminiscent of spinodal decomposition [62] whereby the single phase spontaneously separates uniformly throughout the space into two phases, without the nucleation and growth which normally characterises phase separation. In these conditions, chromatin exhibited the same pattern (Fig. 6b), indicating that Ki-67 overexpression drives heterochromatinisation,

consistent with our earlier findings [58]. We next examined whether Ki-67 mobility is consistent with liquid-like behaviour by Fluorescent Recovery After Photobleaching (FRAP) experiments. We investigated both the recovery of the bleached area of part of a Ki-67-positive compartment, and an adjacent unbleached area of the same compartment. Rapid recovery of the bleached area and preferential mixing of components from the unbleached to the bleached area would be indicative of a liquid-like phase-separated compartment [63]. We performed such FRAP assays on cells with different levels of Ki-67, in interphase, or in mitosis where Ki-67 localises to the PCL. At low expression levels, the recovery half-time was of about 14 seconds, while high expression levels showed a significantly slower recovery. This is consistent with the emerging idea that phase separation may be coupled with percolation, whereby a percolated network of molecules spanning the volume of condensates confers viscoelastic properties [64]. Interestingly, the recovery was extremely rapid in mitosis, of 8 seconds (Fig. 6c, d; Supplementary Movies 1-3). This behaviour indicates liquid-like mixing with an impermeable barrier of the phase-separated compartment [63], and suggests that the perichromosomal layer may be a highly liquid-like phase (Fig. 6c, d; Supplementary Movies 1-3). We further analysed the propensity of Ki-67 to undergo phase separation in cells by using the light-activated Cry2 "optodroplet" system [65] with full length Ki-67 or a series of deletion mutants. Full-length Ki-67 localised to the nucleolus, as expected, but exposure to blue light caused rapid appearance of small round foci in the nucleoplasm, which was dependent on the level of induced Ki-67 expression, consistent with PS (Fig. 6e). These foci showed colocalisation with nucleolin and nucleophosmin (Fig. 6f), intrinsically disordered proteins and interactors of Ki-67 involved in nucleolar organisation, indicating the existence of heterotypic interactions typical of phase-separated MLOs.

We next analysed both by modelling and experiments the consequences of phosphorylation for PS of Ki-67. As shown above, rG-RPA of full length Ki-67 predicted that its complete phosphorylation should promote PS (Fig. 5a), in agreement with Coarse-grained (CG) molecular dynamics (MD) simulation, which showed increased compaction upon phosphorylation (Fig. 7a; Supplementary Movie 4), and with SCDM analysis, which indicated increased intra-chain interactions (Fig. 5b). We next tested effects of CDK-mediated phosphorylation on Ki-67 phase separation propensity using the optodroplet system in cells. To do this, we promoted the CDK-mediated phosphorylation state by treating cells with okadaic acid to inhibit PP2A, that reverses CDK-mediated phosphorylation, or inhibited CDKs with purvalanol A [17]. Even in the absence of blue light, treatment with okadaic acid led to

formation of new Ki-67 foci within the nucleoplasm (Fig. 7b, c), which also incorporated nucleolin and nucleophosmin (Fig. 7d). Therefore, phosphorylation promotes PS of Ki-67 independently of oligomerisation of the Cry2 domain. Conversely, pan-CDK inhibition with purvalanol A prevented induction of foci upon illumination (Fig. 7b, c). These results are consistent with phosphorylation of full-length Ki-67 promoting PS, as predicted by SCDM, rG-RPA and MD. We observed similar behaviour for constructs lacking the C-terminal LR domain, that binds chromatin, or the N-terminal domain, which is required for the nucleolar localisation of Ki-67 (Supplementary Fig. 7a, b), indicating that PS of Ki-67 is an autonomous property of the protein and is not dependent on a specific localisation on chromatin or to the nucleolus.

A recent *in vitro* study using purified peptides corresponding to repeat domains showed that partial phosphorylation by CDKs of one of the Ki-67 repeats, or phospho-mimicking amino acid substitutions, promotes PS, possibly by generating charge blocks [66]. However, rG-RPA and SCDM analysis predicts that the effects of phosphorylation on PS propensity strongly depend on the sequence. To test this, we analysed each repeat individually by rG-RPA and SCDM, and indeed found that effects of phosphorylation were dependent on the particular repeat studied, as illustrated by the behaviour of repeats 1, 3 and 12. Full phosphorylation was predicted to enhance PS for repeat 1 but suppress it for repeat 3 (Supplementary Fig. 8a, b). Furthermore, we observed that phospho-mimicking substitutions, which each add one negative charge, do not recapitulate effects of phosphorylation, which adds two per site, and can even have opposite effects, as seen for repeat 12 (Supplementary Fig. 8a, b). These results indicate that effects of phosphorylation on PS depend on sequence context and phosphorylation stoichiometry.

We hypothesised that, for many IDPs, full site phosphorylation, which is characteristic of mitosis [9], might have different effects on PS from the lower levels of phosphorylation typical of interphase, thereby providing directionality to PS changes during the cell cycle and potentially creating a switch at mitosis. To test this hypothesis, we designed a synthetic IDP constituting a single "consensus" synthetic Ki-67 repeat derived from an alignment of all 16 Ki-67 repeats, in effect constituting a novel IDP and model CDK substrate with multiple potential phosphosites (Supplementary Fig. 9a). We expected that this protein might show a different behaviour from that of the native full-length Ki-67 due to its single valency and distinct sequence context. Indeed, MD simulation (Supplementary Movie 5) showed that the fully phosphorylated single synthetic Ki-67 repeat is less compact (Supplementary Fig. 9b) and

has lower tendency to phase separate (Supplementary Fig. 9c). This behaviour contrasts with full length native Ki-67, where phosphorylation promotes PS. We purified the synthetic repeat as a GFP-tagged polypeptide and phosphorylated it *in vitro* with recombinant CDK complexes. Nuclear Magnetic Resonance spectroscopy showed a reduced amide proton spectral dispersion typical for an IDP and confirmed appearance of at least 7 phosphorylated residues when fully phosphorylated (Fig. 8a), while we mapped 11 phosphorylation sites by phosphoproteomics (Fig. 8b). We next performed *in vitro* phase separation assays and compared both partially and fully phosphorylated forms of the consensus repeat by varying incubation times and the activity of purified CDK complexes (Fig. 8c). The purified synthetic Ki-67 repeat could form droplets, and, as predicted, this was abolished upon full phosphorylation by CDK, whereas partial phosphorylation had no effect (Fig. 8d), suggesting that CDK-mediated phosphorylation acts as a buffered switch for phase separation. To define the properties of this switch, we analysed all 2048 combinations of the 11 phosphorylation sites on this synthetic protein by rG-RPA and SCDM. Strikingly, 1-6 phosphosites enhanced PS propensity while 8-11 phosphosites strongly reduced it (Fig. 8e, top), which was consistent with SCDM analysis (Fig. 8e, bottom). For low and high numbers of phosphosites, the overall behaviour was independent of the specific combination of phosphorylated sites, whereas 7 sites could either enhance or reduce PS propensity, depending on the exact combination. Taken together, our results lend support to our hypothesis whereby CDK-mediated phosphorylation can generate a buffered switch for homotypic interactions that contribute to PS.

Discussion

In this multidisciplinary study, we show *in vivo* that CDK-dependent mitotic phosphorylation occurs synchronously on diverse proteins whose common denominators are a high level of disorder, localisation to MLOs, and multisite phosphorylation. Our data suggest that the majority of cell cycle regulated phosphorylation may be controlling phase separation of components of membraneless organelles. Furthermore, CDK-mediated multisite phosphorylation may act as a phase separation switch promoting an abrupt transition into mitosis.

We first exploited the naturally synchronous cell cycles of *Xenopus laevis* to characterise cell cycle-regulated phosphorylation in single embryos at ultra-high resolution, allowing us to distinguish between progressive phosphorylation where different substrates become

phosphorylated sequentially, as suggested by a model in which a complex combination of features encoded in the amino acid sequence of substrates determines phosphorylation timing [14], from the rapid phosphorylation that might result from the observed switch-like mitotic activation of CDK1 [67]. A previous large-scale analysis of cell cycle-regulated phosphorylation used cell synchronisation procedures (nocodazole, thymidine) to show that potential phosphorylation sites are fully phosphorylated in mitosis [9], but phosphorylation dynamics could not be determined. True cell cycle synchronisation of entire cell populations has been deemed impossible due to differences between cells in the timing of entry into and exit from the blocks [22]. Thus, the rather progressive dynamics of CDK-mediated phosphorylation seen from synchronisation studies in fission yeast [68] may not reflect the behaviour occurring in single cells. Indeed, a comparison of cell cycle-regulated phosphorylation sites derived from synchronised cells [9] or from non-synchronised cells selected by flow cytometry [25] revealed that the synchronisation procedures used previously may artificially select for maximal phosphorylation. The same study [25] also showed that all identified phosphosites that peaked in mitosis displayed similar cell cycle behaviour, but the resolution was not sufficient to distinguish differences in kinetics between different phosphosites; this might be due to the elutriation windows used that, by definition, select similar but not identically sized cells from the population. Thus, our study in single embryos is unique to date, and demonstrates that all mitotic phosphosites observed undergo phosphorylation simultaneously, irrespective of the nature of the substrate. This is not incompatible with differences in affinity of CDK1 for different substrates, since a theoretical consideration of futile cycles demonstrates how graded inputs can generate all-or-nothing outputs [42]. We further show that this switch-like behaviour does not depend on regulated phosphorylation of CDK1 itself, consistent with the observation that tyrosine-15 phosphorylation of CDK1 is downregulated during early embryonic cell cycles [32,41]; instead, it can likely be accounted for by regulation by Greatwall of the phosphatase that reverses CDK-mediated phosphorylation, as well as by phosphorylation of NIPA, which inactivates the SCF ubiquitin ligase that degrades cyclin B in interphase [69].

Second, we reveal an underlying similarity between most cell cycle kinase substrates: they contain a much higher proportion of disordered residues than other phosphoproteins. While it has previously been found that intrinsic disorder generally predicts phosphorylation site localisation for any protein, irrespective of the kinase [43], and it was previously confirmed that CDK sites conform to this rule by tending to cluster in regions of proteins predicted to be disordered [6,44], what distinguishes cell cycle-regulated phosphorylation from other

phosphorylation, and what determines which kinases are involved, has remained unknown. We find that substrates of CDKs, Aurora and Polo-like kinases are far more disordered than the phosphoproteome average. Even when substrates of two kinase families (CDK and MAP kinases) with the same minimal consensus site motif are compared, the CDK substrates have close to twice the disorder of MAP kinase substrates. This further highlights the enrichment for disordered proteins in cell cycle processes, noted recently [8]. Our data also resolve a circularity problem inherent in earlier work: previous observations of enrichment of CDK sites in disordered regions of proteins [6,44] might have a trivial explanation, since the amino acids constituting the consensus site for CDKs (S, T, P, K and R) are already highly enriched in disordered regions. Our bioinformatic approach corrects for this bias and confirms the validity of the previous observations. We propose that cell cycle kinases have been selected by evolution to phosphorylate the most highly disordered proteins of the proteome, and that this necessarily requires several families of kinases, to phosphorylate sites in disordered regions of proteins that are either positively charged at physiological pH (CDKs, Aurora) or negatively charged (PLK), while Aurora and PLK cannot phosphorylate proline-proximal sites.

Our observations that cell cycle kinase substrates are more disordered than other proteins and that they are frequently key components of MLOs lends the hypothesis that phosphorylation of these substrates might regulate MLOs themselves, consistent with the cell cycle-dependent assembly and disassembly of many MLOs. We provide a medium-throughput analysis of effects of phosphorylation on different CDK substrates that substantiates this hypothesis, which could only be achieved by applying a theoretical approach. Molecular dynamics simulations of biomolecules require large computer resources and timescales and are currently essentially unfeasible for modeling phase separation. In contrast, analytical simulations are powerful tools that can predict conformational properties of IDPs and average the ensemble of disordered states that depend on the sequence of IDRs, with high throughput and with minimal computer load [57]. Theoretical models also allow us to systematically vary different inputs, such as post-translational modifications, mutations, salt concentrations and pH to explore their relative contributions. Our calculations with one IDP and solvent predict binary phase diagrams, and the results match our experimental data for the protein that we use to test our hypothesis, Ki-67.

A previous study provided evidence for phospho-regulation of MLOs in mitosis but attributed it to a different kinase, DYRK3 [45]. However, DYRK3 inhibition led to mitotic formation of abnormal hybrid condensates that contained material from various MLOs (splicing speckles,

stress granules and pericentriolar material), but did not prevent the normal breakdown of MLOs such as nucleoli, nuclear pore complexes or Cajal bodies. Our data rather implicate CDK1 as the likely major MLO regulator in mitosis. This is not unprecedented since CDKs can prevent phase separation of components of replication complexes [70], promote nuclear pore disassembly [71] and dissolve stress granules in yeast [72]. We additionally provide evidence that CDK-mediated phosphorylation can both promote or inhibit biological phase separation, depending both on the sequence context and the stoichiometry of phosphorylation. The latter adds an additional switch-like regulation to the onset of mitosis: passing a threshold number of phosphorylations can switch from promoting phase separation to inhibiting it. Thus, our data show that CDK-mediated multisite phosphorylation may act as a buffered switch for phase separation, which is independent of the exact combinations of phosphorylated sites, providing a robust underlying mechanism that may contribute to the abruptness of the cellular reorganisation at the entry into mitosis. Interestingly, phosphosites specific to meiotic M-phase samples appeared to be the most highly phosphorylated, and the most multiphosphorylated peptides were detected in these samples. We speculate that such a prevalence of "hyper-phosphorylation" might reflect the long term maintenance of the M-phase state in unfertilised eggs, and suggest that a more detailed quantitative analysis of the threshold phosphorylation levels required to generate and maintain meiotic versus mitotic M-phase might reveal interesting differences between these two states.

Finally, we provide evidence that the perichromosomal layer of mitotic chromosomes may be liquid, and we suggest a mechanism for mitotic targeting of nucleolar components to the perichromosomal layer by Ki-67 [58,59] via CDK-mediated phosphorylation, which reduces PS propensity of several major nucleolar IDPs, thus triggering nucleolar disassembly, while simultaneously promoting PS of Ki-67 to recruit nucleolar components to chromosomes.

Acknowledgments: We thank Merlijn Witte for technical assistance with the *Xenopus laevis* egg fertilization experiments, Ariane Abrieu for a gift of CSF egg extracts, and Markus Raschle from the Technical University of Kaiserslautern for providing the *Xenopus laevis* protein database, Jonathan Huihui during early phases of theoretical analysis using SCDM, and Damien Coudreuse for critical reading of the manuscript. **Funding:** AJRH and MA acknowledge support from the Horizon 2020 program INFRAIA project Epic-XS (Project 823839) and the NWO funded Netherlands Proteomics Centre through the National Road Map for Large-scale Infrastructures program X-Omics (Project 184.034.019) of the Netherlands

Proteomics Centre. JMV is supported by scholarships from the Ministry of Science and Technology of Costa Rica (MICITT) and the University of Costa Rica (UCR). PK and MV are funded by the Oncode Institute which is financed by the Dutch Cancer Society and by the gravitation program CancerGenomiCs.nl from the Netherlands Organisation for Scientific Research (NWO). DF and LK are Inserm employees. GD is funded by the Institut National de Cancer, France (INCa) PRT-K programme (PRT-K17 n° 2018-023). The Fisher lab is funded by the Ligue Nationale Contre le Cancer, France (EL2018.LNCC/DF) and INCa (PLBIO18-094). The CBS is a member of France-BioImaging (FBI) and the French Infrastructure for Integrated Structural Biology (FRISBI), supported by the French National Research Agency (ANR-10-INBS-04-01 and ANR-10-INBS-05). KG acknowledges support from R01GM138901.

Author contributions: MA and DF conceived and supervised the project. JMV, PK and LK designed and interpreted experiments. JMV, HT, AH, MPh, GvM, CE-R, AF, NAS, EAG, DC, MPa, AB, LK and GD performed experiments and interpreted the data. MV and AC supervised GvM and EAG, respectively. JMV, LK, GD, KG, DF and MA wrote the paper.

Competing interests: Authors declare no competing interests.

Data and materials availability: All data is available in the main text or the supplementary materials. All code and materials are available on request.

Supplementary Materials:

Materials and Methods

Supplementary Fig. 1-9

Supplementary Dataset 1-5

Supplementary Movies 1-5

Figures

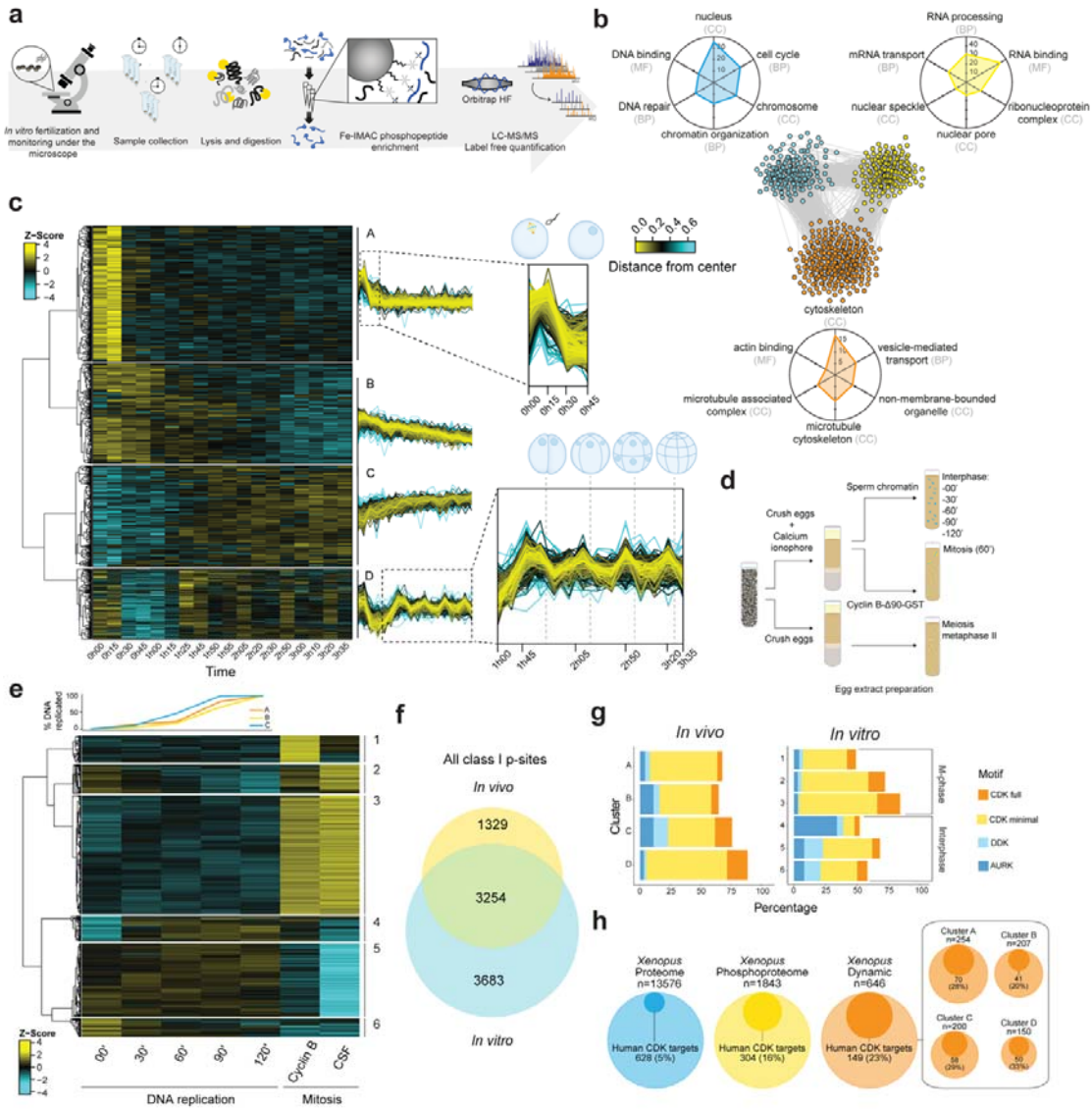

Figure 1. The time-resolved phosphoproteome from a single-cell to a 16-cell embryo and its cell cycle assignment. a. Schematic representation of the workflow. Single *Xenopus* eggs and embryos were collected followed by cell lysis, protein digestion, phosphopeptide enrichment and high-resolution proteomics analysis. **b.** STRING network of functionally associated proteins undergoing dynamic phosphorylation (each node represents a protein). Vicinity clustering reveals three main groups (yellow, blue and orange) with a high degree of association. Radar plots show the corresponding GO terms (adjusted p value <0.05) for each group (axes show -Log_{10}(adj p value) for each GO term). **c.** Hierarchical clustering of significantly changing phosphosites (ANOVA, Benjamini-Hochberg correction, FDR 0.05), reveals 4 clusters with distinct regulation (A-D). Dashed boxes in clusters A and D are zoomed-

in to highlight dynamic phosphorylation patterns (dashed lines depict the time points of cell division). Time point 0h00 corresponds to the unfertilised egg. **d.** Scheme of the experiment in the *Xenopus* egg extract. **e.** Top: quantification of DNA replication in each biological replicate. Below: Hierarchical clustering of dynamic phosphosites (ANOVA, Benjamini-Hochberg correction, FDR 0.05) reveals differential regulation of phosphosites during S-phase and mitosis. **f.** Overlap between *in vivo* (embryo) and *in vitro* (egg extract) phosphoproteomics. **g.** Proportion of phosphosites according to their potential upstream kinase for each cluster in the *in vivo* (left) and *in vitro* (right) experiments. **h.** Circle plots presenting enrichment of homologues of human CDK substrates among *Xenopus* phosphoproteins detected *in vivo* and those with dynamic phosphosites.

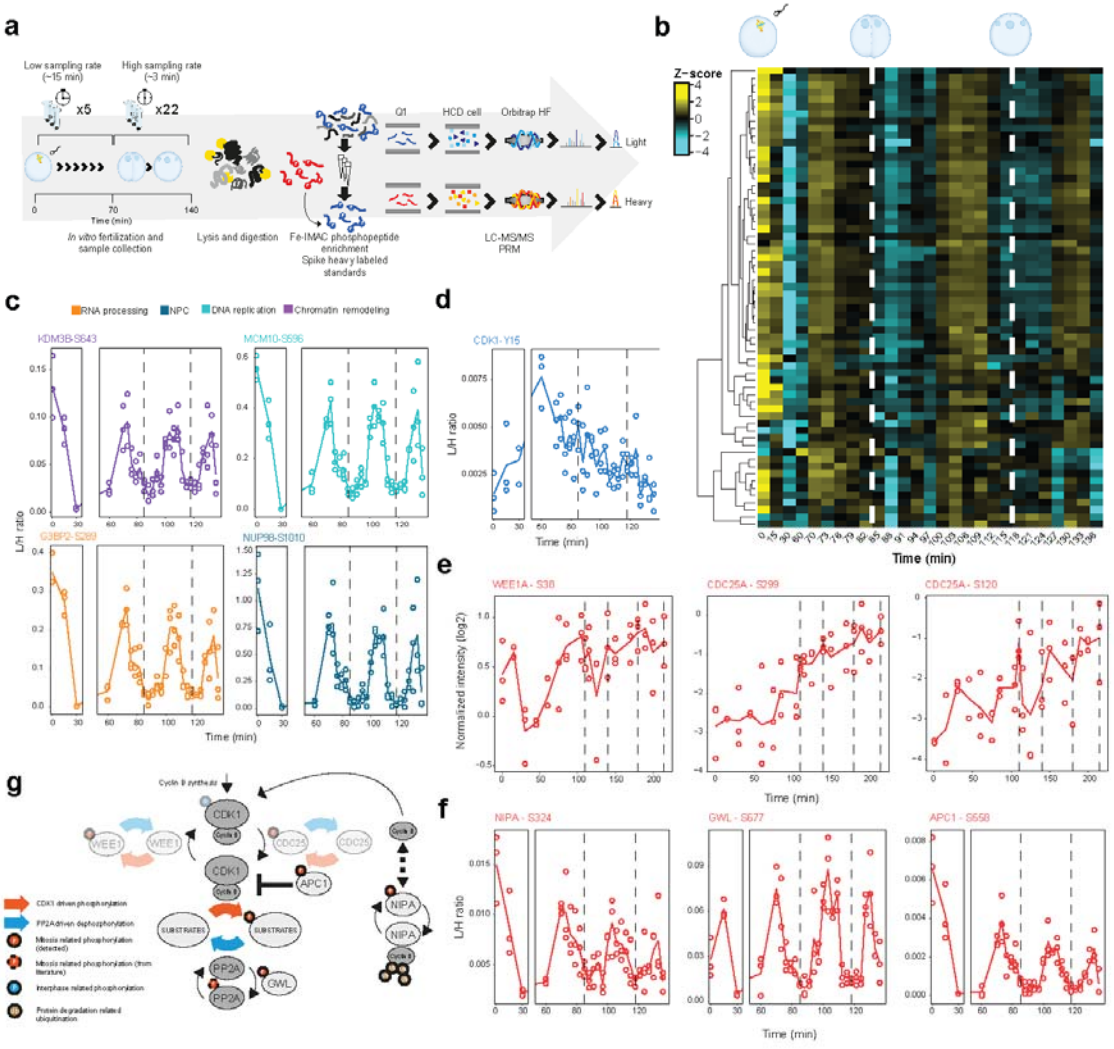

Figure 2. Switch-like mitotic phosphorylation *in vivo*. a. Schematic representation of the workflow for high-time resolution analysis of mitotic phosphosites. Samples were collected

over two cell divisions and enriched phosphopeptides were subjected to targeted proteomics analysis. **b.** Heat map shows a highly synchronous wave of phosphorylation preceding each of the two cell divisions. Dashed lines depict times when cell divisions were recorded. **c.** Single phosphosite plots from selected proteins related to different biological processes. Each dot represents a biological replicate (n=3). Dashed lines depict times when cell divisions were recorded. **d.** Single phosphosite plot of CDK1 inhibitory phosphorylation (Y15). **e-g.** Phosphorylation dynamics of the CDK1-oscillator network. Single phosphosite plots of CDK1 regulators measured by shotgun (**e**) or targeted (**f**) phosphoproteomics. **g.** CDK1-oscillator network: our data suggest that control of cyclin levels via positive (*e.g.* NIPA ubiquitin ligase) and negative (*e.g.* APC) feedback loops, accompanied by PP2A inactivation via GWL, can generate oscillation of CDK1 activity during early cell divisions. CDK1-Y15 regulation via feedback loops consisting of CDC25 and WEE1A (greyed out) seems to be less important for switch-like mitotic phosphorylation after the first cell division.

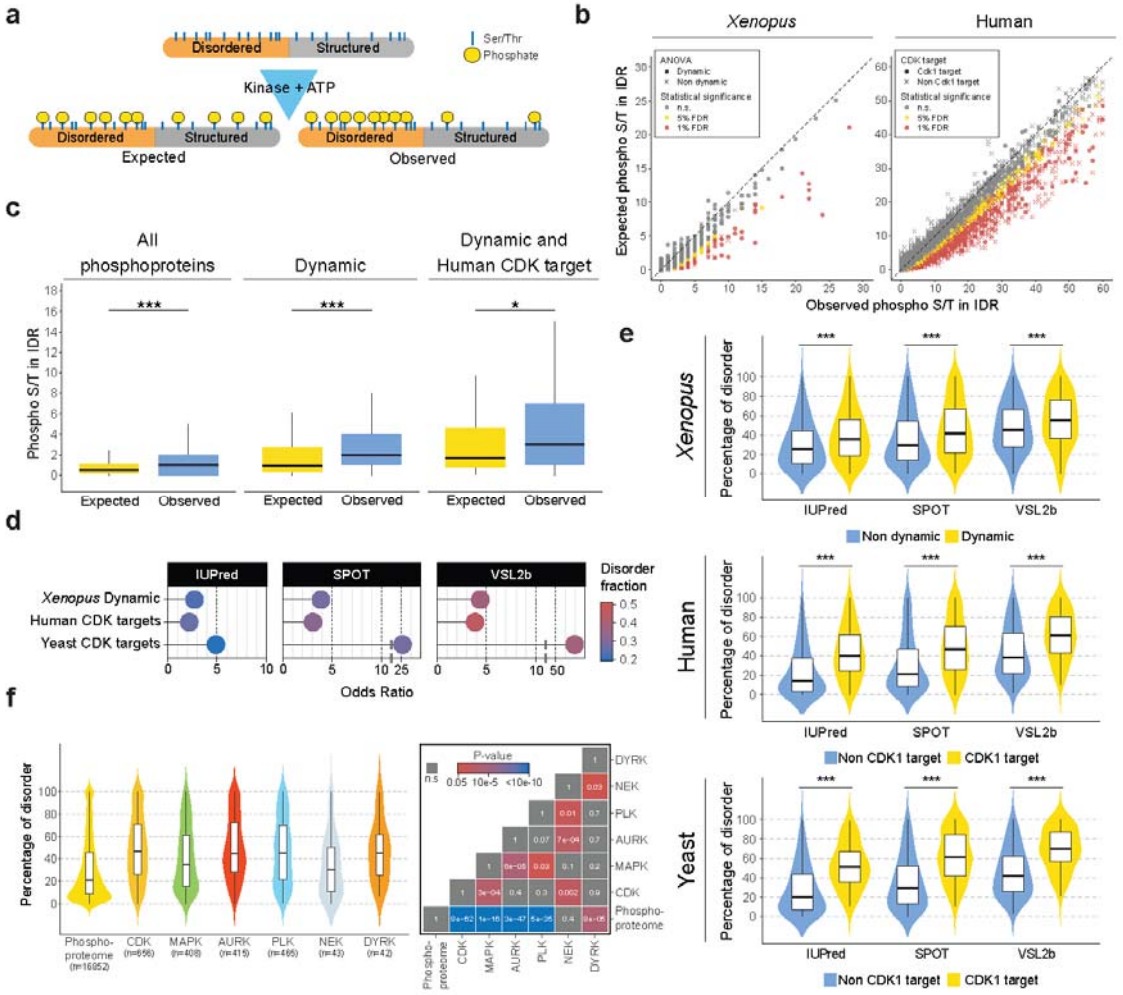

Fig. 3. The cell cycle phosphoproteome is characterised by intrinsic disorder. a. Scheme illustrating hypothetical enrichment of phosphorylation in disordered regions when taking into account amino acid compositional bias. **b.** Scatter plot of expected vs observed phosphorylated Ser/Thr for each protein of human and *Xenopus* phosphoprotein datasets. FDR thresholds of 5% and 1% are marked in yellow and red respectively. Circles: proteins with at least one dynamic phosphorylation in *Xenopus*, or human CDK1 subfamily substrates, respectively. **c.** Boxplots showing expected vs observed phosphorylated Ser/Thr among all phosphoproteins detected (left), phosphoproteins with at least one dynamic phosphosite (middle), and dynamic phosphoproteins also detected as CDK1 subfamily targets in humans (right). Distributions were compared with the Wilcoxon signed-rank test. *$p<0.05$, **$p<0.01$, ***$p<0.001$. **d.** Plots showing the common Odds Ratio of Ser/Thr phosphorylation in structured and disordered regions calculated with the Fisher's test (see Supplementary Fig. 5b, c). For all organisms, the disordered regions were calculated with three different disorder predictors. The disordered fraction is presented in a colour scale. **e.** Violin plots of the distribution of disordered residues per protein for CDK targets vs the rest of the phosphoproteome for human and yeast, and dynamic phosphoproteins vs the rest of the phosphoproteome for *Xenopus*. Intrinsic disorder was calculated with three different predictors (IUPred, SPOT, and VSL2b). Statistical significance was evaluated with the Wilcoxon–Mann–Whitney test; ***$p<0.001$. **f.** Violin plot (left) showing the distribution of disordered residues per protein for CDK, MAPK, Aurora, PLK, NEK and DYRK kinase targets vs the rest of the phosphoproteome for human targets. Statistical significance was assessed by Kruskal-Wallis ANOVA, and pairwise comparisons were performed with Dunn's post-hoc tests. The adjusted p-values (Benjamini-Hochberg) are shown in a tile plot (right).

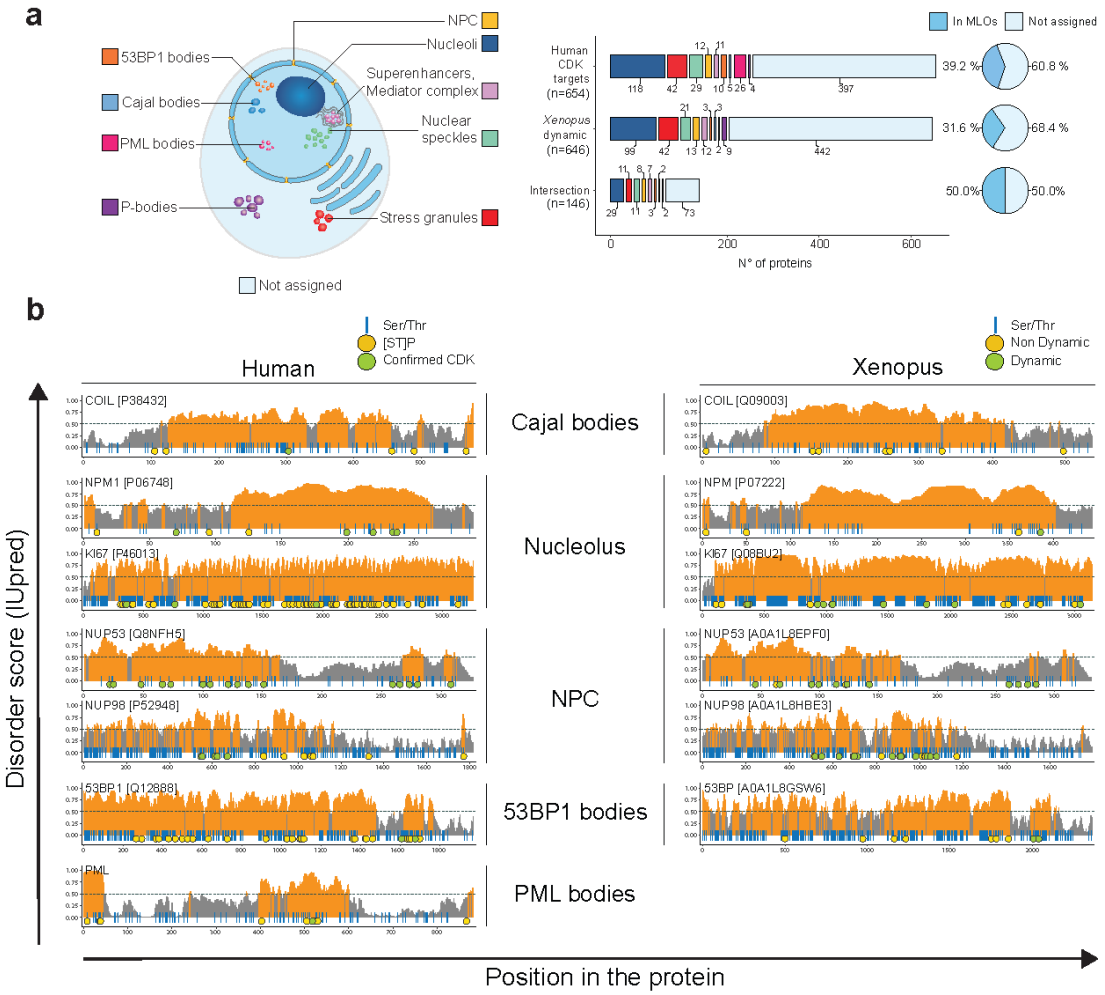

Fig. 4. Cell cycle-regulated phosphorylation of key MLO proteins. a. Human CDK1 subfamily targets, *Xenopus* dynamic phosphoproteins, and the intersection of both sets, that are present in our manually curated proteome of membraneless organelles. **b.** Diagrams of IUPred scores over the length of human CDK targets identified as primary components of MLOs in different studies, and their *Xenopus* homologues in this study. Regions with scores >0.5 (orange) are considered to be disordered, and <0.5 (grey) structured. Blue vertical lines indicate Ser and Thr residues; yellow circles, known Ser/Thr-Pro phosphosites (human) and non-dynamic phosphosites (*Xenopus*); green circles, confirmed CDK1 subfamily phosphorylations (human) and dynamic phosphorylations (*Xenopus*), from both embryos and egg extracts.

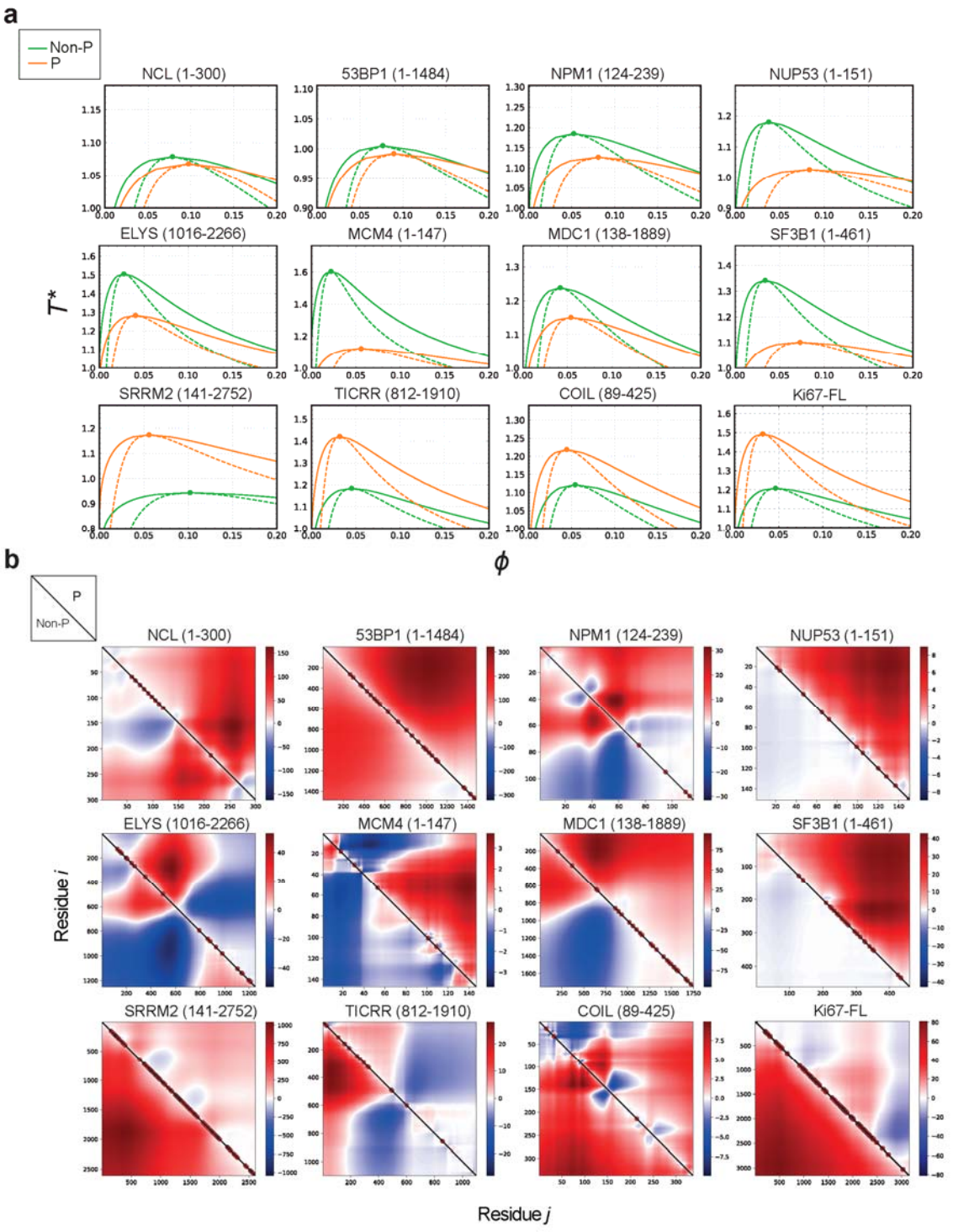

Fig. 5. CDK-mediated phosphorylation regulates phase separation propensity of major MLO components. a. Temperature-density phase diagrams for the phosphorylated (P, in orange) and non-phosphorylated (Non-P, in green) forms of a selection of human CDK targets and major MLO components. Any point within the coexistence region (bounded by the solid line) will phase separate into a dilute and dense phase whose density is given by the values on

the phase boundary. Points within the spinodal line (in dash) will spontaneously phase separate into dilute and dense phases without going through the process of nucleation. Circles denote critical temperature and density which is also the location where the coexistence and spinodal curves meet. For temperature above the critical value, there is no phase separation. **b.** Sequence Charge Decoration Matrix (SCDM) maps for the proteins in (a) (IDRs analysed are indicated), depicting the contribution of electrostatic interaction dictating the distance between two amino acid residues i and j (shown in x and y axes). The values of SCDM for different residue pairs (i,j) are shown using colour schemes with red and blue denoting positive (repulsive) and negative (attractive) values, respectively. The lower and upper triangles indicate SCDM map for the unphosphorylated (non-P) and phosphorylated (P) sequences, respectively. Confirmed and putative (Ser/Thr-Pro) CDK phosphorylation sites were taken into account for the analysis and are indicated with red circles.

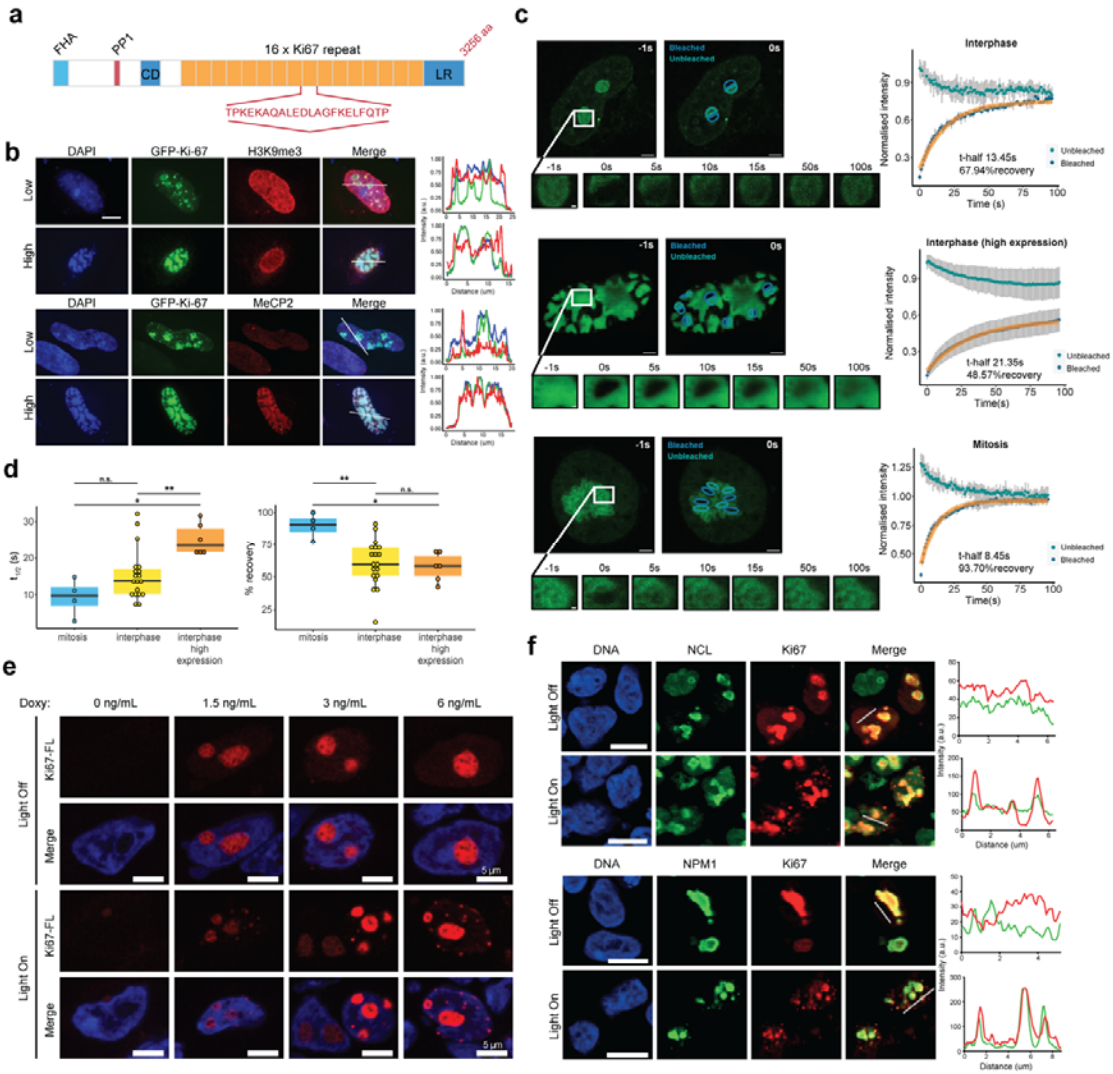

Fig. 6. The model CDK substrate Ki-67 forms biomolecular condensates in cells.

a. Scheme of the human Ki-67 protein (FHA, forkhead-associated domain; PP1, PP1 phosphatase-binding domain; CD, conserved domain; LR, leucine arginine-rich domain). Highlighted, Ki-67 repeat consensus motif. **b.** Cells expressing full-length Ki-67 at different levels show evidence for phase separation; at low levels Ki-67 is predominantly nucleolar but also forms foci in nucleoplasm that recruit heterochromatin, as indicated by H3K9me3 staining; at high levels Ki-67 partitions the entire nucleus into two phases, a Ki-67-dense phase that induces global heterochromatin formation marked by H3K9me3 and MeCP2. DNA was stained with DAPI. Scale bar, 10 µm. **c.** FRAP of Ki-67 shows liquid-like behaviour. Left: representative images of cells expressing different levels of Ki-67 in interphase (top, middle) and in mitosis where Ki-67 localises to the perichromosomal layer (bottom) showing bleached regions and contiguous non-bleached regions; just before (left) and after (right) bleaching.

Scale bars, 3µm. Insets: images of Ki-67 fluorescence at different recovery times after bleaching. Scale bars, 0.5 µm. Right: average fluorescence intensity values over time for bleached (dark blue) and unbleached (teal blue) regions. Orange, non-linear regression fitting of the data. **d.** Left: boxplot of the average recovery half-time for each cell, grouped by category of Ki-67 expression: mitosis (n=4), interphase medium-low expression (n=19) and interphase high expression (n=6). Right: boxplot of the average percentage of recovery for each cell, grouped by category of Ki-67 expression: mitosis (n=4), interphase medium-low expression (n=19) and interphase high expression (n=6). **= $p<0.01$ (Wilcoxon test). **e.** Optogenetic induction of Ki-67 biomolecular condensates. Representative fluorescent images of HEK-293 cells expressing opto-Ki-67 (FL) construct, induced by the indicated concentrations of doxycycline (Doxy), before (Light Off) and after (Light On) exposure to blue light. DNA was stained with Hoechst 33258. **f.** Left, representative fluorescent images of U2OS cells expressing opto-Ki-67 construct (full length protein) before (Light Off) and after (Light On) exposure to blue light. Additional staining for nucleolar proteins nucleolin (NCL, top) and nucleophosmin (NPM1, bottom) was performed and colocalisation with Ki-67 assessed (right). DNA was stained with Hoechst 33258; scale bars, 10 µm.

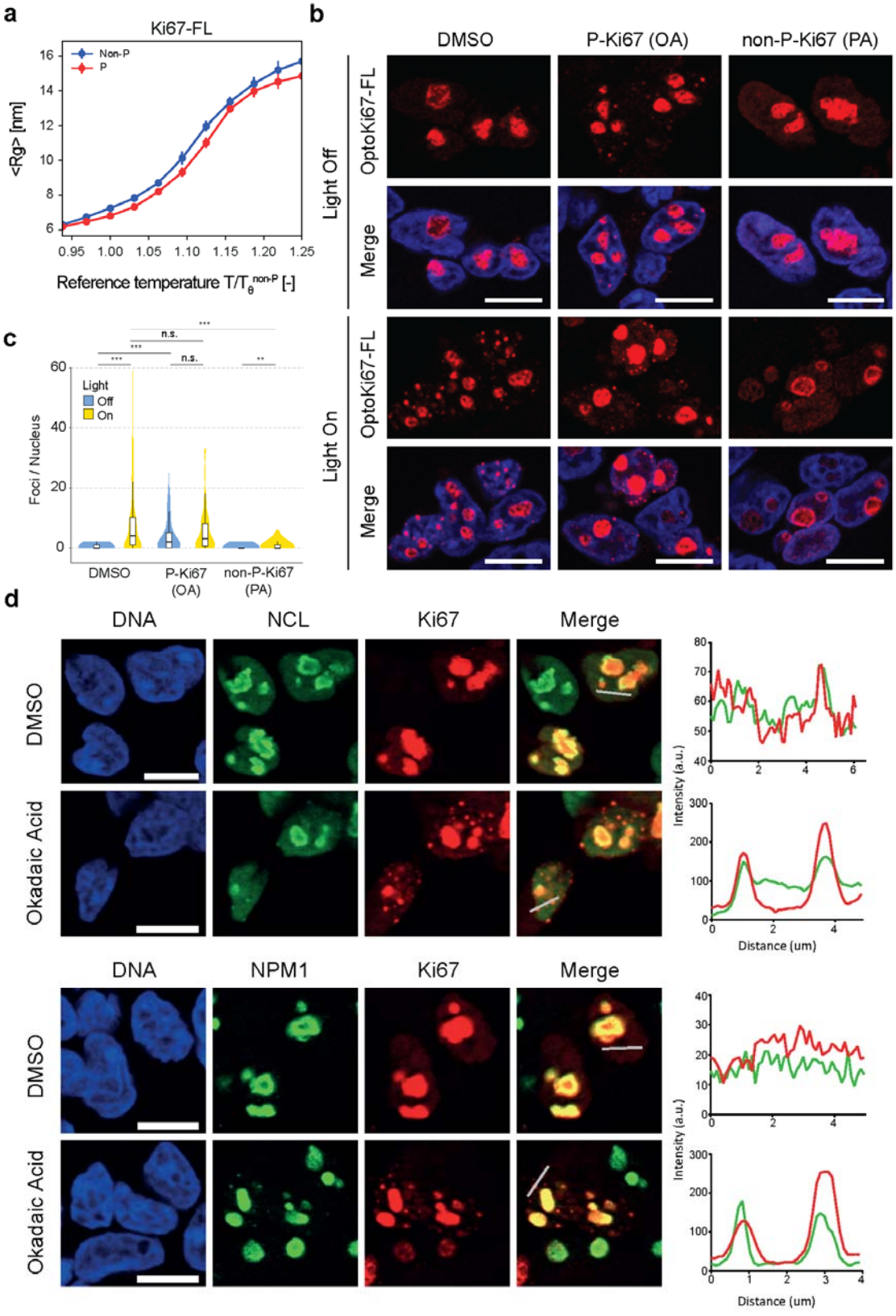

669

670 **Fig. 7. Phosphorylation promotes phase separation of Ki-67. a.** Coarse-grained single-chain

671 MD simulations for full chain Ki-67 showing dependency of the radius of gyration (Rg) on the

simulation temperature. The reference temperature is the θ temperature of the non-phosphorylated molecule. Reported error bars are obtained by block analysis over 10 blocks. **b.** Representative fluorescent images of HEK-293 cells expressing opto-Ki-67 (FL) construct before (Light Off) and after (Light On) exposure to blue light. Cells were pretreated for 1h with either vehicle (DMSO), 0.5 µM okadaic acid (OA), to inhibit protein phosphatase 2A, or 5 µM purvalanol A (PA), to inhibit CDKs. DNA was stained with Hoechst 33258; scale bars, 10µm. **c.** Violin plot presenting quantification of results from (b); the number of foci per nucleus was counted. Statistical significance was assessed by one-way ANOVA on ranks (Kruskal–Wallis test) and pairwise post-hoc comparisons using the Mann–Whitney test. P-values were adjusted by the Benjamini-Hochberg method. **d.** Phosphorylation-induced Ki-67 foci are biological condensates. Cells were treated for 1h with either vehicle (DMSO) or 0.5 µM okadaic acid (OA), to inhibit protein phosphatase 2A. Additional staining for nucleolar proteins nucleolin (NCL) and nucleophosmin (NPM1) was performed and colocalisation with Ki-67 foci assessed (right). DNA was stained with Hoechst 33258; scale bars, 10 µm.

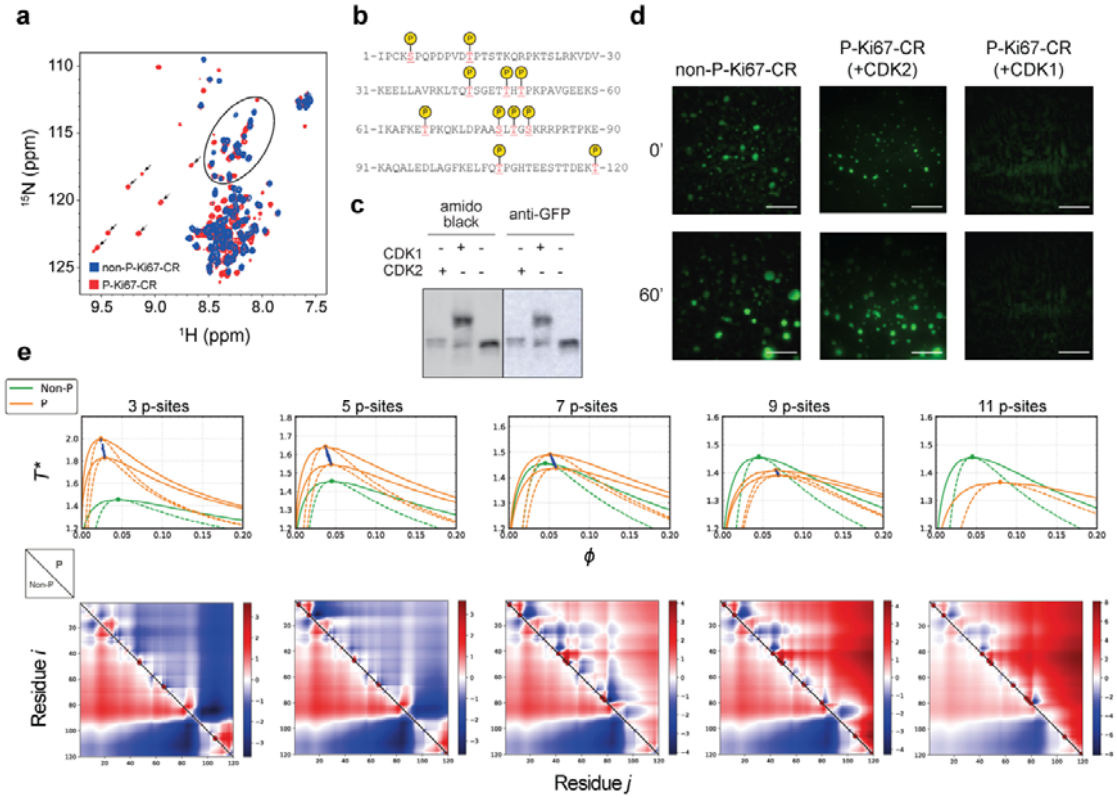

Fig. 8. CDK-mediated phosphorylation can generate a buffered phase separation switch. **a.** Overlaid NMR ^{1}H-^{15}N HSQC of unphosphorylated (blue) and CDK-phosphorylated (red) GFP-tagged Ki-67 consensus repeat. Each cross-peak corresponds to one residue. The seven

new deshielded cross peaks (highlighted by a black flag) appearing above 8.5 ppm in ^{1}H correspond to phosphorylated serines or threonines (^{1}H downfield chemical shift perturbation on phosphorylated Ser/Thr residues due to phosphate electronegativity). Non phosphorylated Ser/Thr residues are surrounded by a black oval. **b, c.** GFP-Ki-67 consensus repeat was phosphorylated *in vitro* using recombinant CDK1-cyclin B-CKS1 or CDK2-cyclin A protein complexes and the phosphosites were mapped by mass-spectrometry (b) and the stoichiometry of phosphorylation was analysed by Phos-Tag SDS-PAGE (c) (amidoblack staining was used as loading control). **d.** Representative fluorescence images of *in vitro* phase separation assay with purified GFP-tagged Ki-67 consensus repeat (CR), non-phosphorylated (non-P) or *in vitro* phosphorylated (P) with recombinant CDK1-cyclin B-CKS1 or CDK2-cyclin A, at indicated time points; scale bars, 10μm. **e.** Top, temperature-density phase diagrams for the consensus repeat sequence of Ki-67. Critical temperature and density (blue circles) were computed for all possible 2048 sequences that arise from different degrees of phosphorylation. For a given degree of phosphorylation there are multiple possible sequences, of which two were chosen, corresponding to the highest and lowest values of the critical point. For these, temperature-dependent (in reduced unit) phase diagrams (solid orange) and spinodal lines (dashed orange) are shown along with the unmodified sequence (in green). Only critical points (blue circles) are presented for all the other sequences for a given stoichiometry/degree of phosphorylation. Bottom, SCDM maps of the unmodified sequence (Non-P, lower triangle) and a specific phosphorylated sequence (P, upper triangle). The phosphorylated sequence for a given stoichiometry (degree of phosphorylation) was chosen by selecting the sequence with the corresponding critical temperature and density closest to the average of the highest and lowest critical points. SCDM and Phase diagrams are consistent and show that phosphorylation can lower propensity to phase separate when eight or more sites are phosphorylated, contrary to sequences where six or less sites are phosphorylated.

References

1. Hyman, A. A. Whither systems biology. *Philos. Trans. R. Soc. Lond. B Biol. Sci.* **366**, 3635–3637 (2011).
2. Errico, A., Deshmukh, K., Tanaka, Y., Pozniakovsky, A. & Hunt, T. Identification of substrates for cyclin dependent kinases. *Adv. Enzyme Regul.* **50**, 375–399 (2010).
3. Ubersax, J. A. *et al.* Targets of the cyclin-dependent kinase Cdk1. *Nature* **425**, 859–64 (2003).
4. Chi, Y. *et al.* Identification of CDK2 substrates in human cell lysates. *Genome Biol.* **9**, R149 (2008).

5. Blethrow, J. D., Glavy, J. S., Morgan, D. O. & Shokat, K. M. Covalent capture of kinase-specific phosphopeptides reveals Cdk1-cyclin B substrates. *Proc. Natl. Acad. Sci. U.S.A.* **105**, 1442–7 (2008).
6. Holt, L. J. *et al.* Global analysis of Cdk1 substrate phosphorylation sites provides insights into evolution. *Science* **325**, 1682–6 (2009).
7. Michowski, W. *et al.* Cdk1 Controls Global Epigenetic Landscape in Embryonic Stem Cells. *Mol. Cell* **78**, 459-476.e13 (2020).
8. Mahdessian, D. *et al.* Spatiotemporal dissection of the cell cycle with single-cell proteogenomics. *Nature* **590**, 649–654 (2021).
9. Olsen, J. V. *et al.* Quantitative phosphoproteomics reveals widespread full phosphorylation site occupancy during mitosis. *Sci. Signal.* **3**, ra3 (2010).
10. Zegerman, P. & Diffley, J. F. Phosphorylation of Sld2 and Sld3 by cyclin-dependent kinases promotes DNA replication in budding yeast. *Nature* **445**, 281–5 (2007).
11. Tanaka, S. *et al.* CDK-dependent phosphorylation of Sld2 and Sld3 initiates DNA replication in budding yeast. *Nature* **445**, 328–32 (2007).
12. Orlicky, S., Tang, X., Willems, A., Tyers, M. & Sicheri, F. Structural basis for phosphodependent substrate selection and orientation by the SCFCdc4 ubiquitin ligase. *Cell* **112**, 243–256 (2003).
13. Nash, P. *et al.* Multisite phosphorylation of a CDK inhibitor sets a threshold for the onset of DNA replication. *Nature* **414**, 514–21 (2001).
14. Örd, M. *et al.* Multisite phosphorylation code of CDK. *Nat. Struct. Mol. Biol.* **26**, 649–658 (2019).
15. Coudreuse, D. & Nurse, P. Driving the cell cycle with a minimal CDK control network. *Nature* **468**, 1074–1079 (2010).
16. Basu, S., Greenwood, J., Jones, A. W. & Nurse, P. Core control principles of the eukaryotic cell cycle. *Nature* **607**, 381-386 (2022).
17. Krasinska, L. *et al.* Protein Phosphatase 2A Controls the Order and Dynamics of Cell-Cycle Transitions. *Mol. Cell* **44**, 437–50 (2011).
18. Gavet, O. & Pines, J. Progressive activation of CyclinB1-Cdk1 coordinates entry to mitosis. *Dev. Cell* **18**, 533–43 (2010).
19. Purvis, J. E. & Lahav, G. Encoding and decoding cellular information through signaling dynamics. *Cell* **152**, 945–956 (2013).

20. Budnik, B., Levy, E., Harmange, G. & Slavov, N. SCoPE-MS: mass spectrometry of single mammalian cells quantifies proteome heterogeneity during cell differentiation. *Genome Biol.* **19**, 161 (2018).
21. Lombard-Banek, C., Moody, S. A., Manzini, M. C. & Nemes, P. Microsampling Capillary Electrophoresis Mass Spectrometry Enables Single-Cell Proteomics in Complex Tissues: Developing Cell Clones in Live Xenopus laevis and Zebrafish Embryos. *Anal. Chem.* **91**, 4797–4805 (2019).
22. Cooper, S. The synchronization manifesto: a critique of whole-culture synchronization. *FEBS J.* **286**, 4650–4656 (2019).
23. Ly, T., Endo, A. & Lamond, A. I. Proteomic analysis of the response to cell cycle arrests in human myeloid leukemia cells. *eLife* **4**, e04534 (2015).
24. Ly, T. *et al.* A proteomic chronology of gene expression through the cell cycle in human myeloid leukemia cells. *eLife* **3**, e01630 (2014).
25. Ly, T. *et al.* Proteomic analysis of cell cycle progression in asynchronous cultures, including mitotic subphases, using PRIMMUS. *eLife* **6**, e27574 (2017).
26. Newport, J. & Kirschner, M. A major developmental transition in early Xenopus embryos: I. characterization and timing of cellular changes at the midblastula stage. *Cell* **30**, 675–686 (1982).
27. Newport, J. W. & Kirschner, M. W. Regulation of the cell cycle during early Xenopus development. *Cell* **37**, 731–42 (1984).
28. Post, H. *et al.* Robust, Sensitive, and Automated Phosphopeptide Enrichment Optimized for Low Sample Amounts Applied to Primary Hippocampal Neurons. *J. Proteome Res.* **16**, 728–737 (2017).
29. Presler, M. *et al.* Proteomics of phosphorylation and protein dynamics during fertilization and meiotic exit in the Xenopus egg. *Proc. Natl. Acad. Sci. U.S.A.* **114**, E10838–E10847 (2017).
30. Clift, D. & Schuh, M. Restarting life: fertilization and the transition from meiosis to mitosis. *Nat. Rev. Mol. Cell Biol.* **14**, 549–562 (2013).
31. Peuchen, E. H. *et al.* Phosphorylation Dynamics Dominate the Regulated Proteome during Early Xenopus Development. *Sci. Rep.* **7**, 15647 (2017).
32. Ferrell, J. E., Jr., Wu, M., Gerhart, J. C. & Martin, G. S. Cell cycle tyrosine phosphorylation of p34cdc2 and a microtubule-associated protein kinase homolog in Xenopus oocytes and eggs. *Mol. Cell. Biol.* **11**, 1965–71 (1991).

33. Songyang, Z. *et al.* A structural basis for substrate specificities of protein Ser/Thr kinases: primary sequence preference of casein kinases I and II, NIMA, phosphorylase kinase, calmodulin-dependent kinase II, CDK5, and Erk1. *Mol. Cell. Biol*. **16**, 6486–6493 (1996).
34. Suzuki, K. *et al.* Identification of non-Ser/Thr-Pro consensus motifs for Cdk1 and their roles in mitotic regulation of C2H2 zinc finger proteins and Ect2. *Sci. Rep.* **5**, 7929 (2015).
35. Lawrence, R. T., Searle, B. C., Llovet, A. & Villén, J. Plug-and-play analysis of the human phosphoproteome by targeted high-resolution mass spectrometry. *Nat. Methods* **13**, 431–434 (2016).
36. Schmidlin, T. *et al.* Assessment of SRM, MRM3, and DIA for the targeted analysis of phosphorylation dynamics in non-small cell lung cancer. *Proteomics* **16**, 2193–2205 (2016).
37. Schmidlin, T. *et al.* High-Throughput Assessment of Kinome-wide Activation States. *Cell Systems* **9**, 366-374.e5 (2019).
38. Peterson, A. C., Russell, J. D., Bailey, D. J., Westphall, M. S. & Coon, J. J. Parallel Reaction Monitoring for High Resolution and High Mass Accuracy Quantitative, Targeted Proteomics *. *Mol. Cell. Proteomics* **11**, 1475–1488 (2012).
39. Rankin, S. & Kirschner, M. W. The surface contraction waves of Xenopus eggs reflect the metachronous cell-cycle state of the cytoplasm. *Curr. Biol.* **7**, 451–4 (1997).
40. Perez-Mongiovi, D., Chang, P. & Houliston, E. A propagated wave of MPF activation accompanies surface contraction waves at first mitosis in Xenopus. *J. Cell Sci.* **111**, 385–393 (1998).
41. Tsai, T. Y.-C., Theriot, J. A. & Jr, J. E. F. Changes in Oscillatory Dynamics in the Cell Cycle of Early Xenopus laevis Embryos. *PLoS Biol.* **12**, e1001788 (2014).
42. Goldbeter, A. & Koshland, D. E., Jr. An amplified sensitivity arising from covalent modification in biological systems. *Proc. Natl. Acad. Sci. U. S. A.* **78**, 6840–4 (1981).
43. Iakoucheva, L. M. *et al.* The importance of intrinsic disorder for protein phosphorylation. *Nucleic Acids Res.* **32**, 1037–1049 (2004).
44. Moses, A. M., Hériché, J.-K. & Durbin, R. Clustering of phosphorylation site recognition motifs can be exploited to predict the targets of cyclin-dependent kinase. *Genome Biol.* **8**, R23 (2007).
45. Rai, A. K., Chen, J.-X., Selbach, M. & Pelkmans, L. Kinase-controlled phase transition of membraneless organelles in mitosis. *Nature* **559**, 211–216 (2018).
46. Shimobayashi, S. F., Ronceray, P., Sanders, D. W., Haataja, M. P. & Brangwynne, C. P. Nucleation landscape of biomolecular condensates. *Nature* **599**, 503–506 (2021).

47. Berchtold, D., Battich, N. & Pelkmans, L. A Systems-Level Study Reveals Regulators of Membrane-less Organelles in Human Cells. *Mol. Cell* **72**, 1035-1049.e5 (2018).
48. Hur, W. *et al.* CDK-Regulated Phase Separation Seeded by Histone Genes Ensures Precise Growth and Function of Histone Locus Bodies. *Dev. Cell* **54**, 379-394.e6 (2020).
49. Sridharan, S. *et al.* Systematic discovery of biomolecular condensate-specific protein phosphorylation. *Nat. Chem. Biol.* **18**, 1104–1114 (2022).
50. van Mierlo, G. *et al.* Predicting protein condensate formation using machine learning. *Cell Rep.* **34**, 108705 (2021).
51. Lin, Y.-H., Wu, H., Jia, B., Zhang, M. & Chan, H. S. Assembly of model postsynaptic densities involves interactions auxiliary to stoichiometric binding. *Biophys. J.* **121**, 157–171 (2022).
52. Ghosh, K. Stoichiometric versus stochastic interaction in models of liquid-liquid phase separation. *Biophys. J.* **121**, 4–6 (2022).
53. Kim, T. H. *et al.* Phospho-dependent phase separation of FMRP and CAPRIN1 recapitulates regulation of translation and deadenylation. *Science* **365**, 825–829 (2019).
54. Lin, Y.-H., Brady, J. P., Chan, H. S. & Ghosh, K. A unified analytical theory of heteropolymers for sequence-specific phase behaviors of polyelectrolytes and polyampholytes. *J. Chem. Phys.* **152**, 045102 (2020).
55. Huihui, J. & Ghosh, K. An analytical theory to describe sequence-specific inter-residue distance profiles for polyampholytes and intrinsically disordered proteins. *J. Chem. Phys.* **152**, 161102 (2020).
56. Huihui, J. & Ghosh, K. Intrachain interaction topology can identify functionally similar intrinsically disordered proteins. *Biophys. J.* **120**, 1860–1868 (2021).
57. Ghosh, K., Huihui, J., Phillips, M. & Haider, A. Rules of Physical Mathematics Govern Intrinsically Disordered Proteins. *Annu. Rev. Biophys.* **51**, 355–376 (2022).
58. Sobecki, M. *et al.* The cell proliferation antigen Ki-67 organises heterochromatin. *eLife* **5**, e13722 (2016).
59. Booth, D. G. *et al.* Ki-67 is a PP1-interacting protein that organises the mitotic chromosome periphery. *eLife* **3**, e01641 (2014).
60. Hayashi, Y., Kato, K. & Kimura, K. The hierarchical structure of the perichromosomal layer comprises Ki67, ribosomal RNAs, and nucleolar proteins. *Biochem. Biophy. Res. Commun.* **493**, 1043–1049 (2017).
61. Hégarat, N. *et al.* Cyclin A triggers Mitosis either via the Greatwall kinase pathway or Cyclin B. *EMBO J.* **39**, e104419 (2020).

62. Bracha, D. *et al.* Mapping Local and Global Liquid Phase Behavior in Living Cells Using Photo-Oligomerizable Seeds. *Cell* **175**, 1467-1480.e13 (2018).
63. Erdel, F. *et al.* Mouse Heterochromatin Adopts Digital Compaction States without Showing Hallmarks of HP1-Driven Liquid-Liquid Phase Separation. *Mol. Cell* **78**, 236-249.e7 (2020).
64. Mittag, T. & Pappu, R. V. A conceptual framework for understanding phase separation and addressing open questions and challenges. *Mol. Cell* **82**, 2201–2214 (2022).
65. Shin, Y. *et al.* Spatiotemporal Control of Intracellular Phase Transitions Using Light-Activated optoDroplets. *Cell* **168**, 159-171.e14 (2017).
66. Yamazaki, H., Takagi, M., Kosako, H., Hirano, T. & Yoshimura, S. H. Cell cycle-specific phase separation regulated by protein charge blockiness. *Nat. Cell Biol.* **24**, 625–632 (2022).
67. Rata, S. *et al.* Two Interlinked Bistable Switches Govern Mitotic Control in Mammalian Cells. *Curr. Biol.* **28**, 3824-3832.e6 (2018).
68. Swaffer, M. P., Jones, A. W., Flynn, H. R., Snijders, A. P. & Nurse, P. CDK Substrate Phosphorylation and Ordering the Cell Cycle. *Cell* **167**, 1750-1761.e16 (2016).
69. Bassermann, F. *et al.* Multisite phosphorylation of nuclear interaction partner of ALK (NIPA) at G2/M involves cyclin B1/Cdk1. *J. Biol. Chem.* **282**, 15965–15972 (2007).
70. Parker, M. W. *et al.* A new class of disordered elements controls DNA replication through initiator self-assembly. *eLife* **8**, (2019).
71. Laurell, E. *et al.* Phosphorylation of Nup98 by multiple kinases is crucial for NPC disassembly during mitotic entry. *Cell* **144**, 539–550 (2011).
72. Yahya, G. *et al.* Stress granules display bistable dynamics modulated by Cdk. *J. Cell Biol.* **220**, (2021).
73. Parisis, N. *et al.* Initiation of DNA replication requires actin dynamics and formin activity. *EMBO J.* (2017) doi:10.15252/embj.201796585.
74. Lindeboom, R. G. H., Smits, A. H., Perino, M., Veenstra, G. J. C. & Vermeulen, M. Mass Spectrometry-Based Absolute Quantification of Single Xenopus Embryo Proteomes. *Cold Spring Harb. Protoc.* (2018) doi:10.1101/pdb.prot098376.
75. Wisniewski, J. R., Zougman, A., Nagaraj, N. & Mann, M. Universal sample preparation method for proteome analysis. *Nat. Methods* **6**, 359–62 (2009).
76. Meiring, H. D., van der Heeft, E., ten Hove, G. J. & de Jong, A. P. J. M. Nanoscale LC-MS(n): technical design and applications to peptide and protein analysis. *J. Sep. Sci.* **25**, 557–568 (2002).

77. Cox, J. & Mann, M. MaxQuant enables high peptide identification rates, individualized p.p.b.-range mass accuracies and proteome-wide protein quantification. *Nat. Biotechnol.* **26**, 1367–1372 (2008).
78. Temu, T., Mann, M., Raschle, M. & Cox, J. Homology-driven assembly of NOn-redundant protEin sequence sets (NOmESS) for mass spectrometry. *Bioinformatics* **32**, 1417–9 (2016).
79. Tyanova, S. *et al.* The Perseus computational platform for comprehensive analysis of (prote)omics data. *Nat. Methods* **13**, 731–40 (2016).
80. Gu, Z., Eils, R. & Schlesner, M. Complex heatmaps reveal patterns and correlations in multidimensional genomic data. *Bioinformatics* **32**, 2847–2849 (2016).
81. Szklarczyk, D. *et al.* STRING v11: protein-protein association networks with increased coverage, supporting functional discovery in genome-wide experimental datasets. *Nucleic Acids Res.* **47**, D607–D613 (2019).
82. Su, G., Kuchinsky, A., Morris, J. H., States, D. J. & Meng, F. GLay: community structure analysis of biological networks. *Bioinformatics* **26**, 3135–7 (2010).
83. Maere, S., Heymans, K. & Kuiper, M. BiNGO: a Cytoscape plugin to assess overrepresentation of gene ontology categories in biological networks. *Bioinformatics* **21**, 3448–9 (2005).
84. Supek, F., Bosnjak, M., Skunca, N. & Smuc, T. REVIGO summarizes and visualizes long lists of gene ontology terms. *PLoS One* **6**, e21800 (2011).
85. MacLean, B. *et al.* Skyline: an open source document editor for creating and analyzing targeted proteomics experiments. *Bioinformatics* **26**, 966–8 (2010).
86. Wickham, H. *et al.* Welcome to the Tidyverse. *J. Open Source Soft.* **4**, 1686 (2019).
87. Hornbeck, P. V. *et al.* PhosphoSitePlus, 2014: mutations, PTMs and recalibrations. *Nucleic Acids Res.* **43**, D512–D520 (2015).
88. Orthwein, A. *et al.* Mitosis Inhibits DNA Double-Strand Break Repair to Guard Against Telomere Fusions. *Science* **344**, 189–193 (2014).
89. Wyatt, H. D. M., Sarbajna, S., Matos, J. & West, S. C. Coordinated Actions of SLX1-SLX4 and MUS81-EME1 for Holliday Junction Resolution in Human Cells. *Mol. Cell* **52**, 234–247 (2013).
90. Linder, M. I. *et al.* Mitotic Disassembly of Nuclear Pore Complexes Involves CDK1- and PLK1-Mediated Phosphorylation of Key Interconnecting Nucleoporins. *Dev. Cell* **43**, 141-156.e7 (2017).
91. Liu, J. *et al.* Cell cycle-dependent localization of the CDK2-cyclin E complex in Cajal (coiled) bodies. *J Cell Sci.* **113**, 1543–1552 (2000).

92. Chi, Y. *et al.* A novel landscape of nuclear human CDK2 substrates revealed by in situ phosphorylation. *Sci. Adv.* **6**, eaaz9899 (2020).
93. Klein, U. R., Haindl, M., Nigg, E. A. & Muller, S. RanBP2 and SENP3 Function in a Mitotic SUMO2/3 Conjugation-Deconjugation Cycle on Borealin. *Mol. Biol. Cell* **20**, 410–418 (2008).
94. Goto, H. *et al.* Complex formation of Plk1 and INCENP required for metaphase–anaphase transition. *Nat. Cell Biol.* **8**, 180–187 (2006).
95. Bartsch, O., Horstmann, S., Toprak, K., Klempnauer, K.-H. & Ferrari, S. Identification of cyclin A/Cdk2 phosphorylation sites in B-Myb. *Eur. J. Biochem.* **260**, 384–391 (1999).
96. Curtis, M., Nikolopoulos, S. N. & Turner, C. E. Actopaxin is phosphorylated during mitosis and is a substrate for cyclin B1/cdc2 kinase. *Biochem. J.* **363**, 233–242 (2002).
97. Fourest-Lieuvin, A. *et al.* Microtubule Regulation in Mitosis: Tubulin Phosphorylation by the Cyclin-dependent Kinase Cdk1. *Mol. Biol. Cell* **17**, 1041 (2006).
98. Milner, R. E., Busaan, J. L., Holmes, C. F., Wang, J. H. & Michalak, M. Phosphorylation of dystrophin. The carboxyl-terminal region of dystrophin is a substrate for in vitro phosphorylation by p34cdc2 protein kinase. *J. Biol. Chem.* **268**, 21901–21905 (1993).
99. Lowe, M. *et al.* Cdc2 Kinase Directly Phosphorylates the cis-Golgi Matrix Protein GM130 and Is Required for Golgi Fragmentation in Mitosis. *Cell* **94**, 783–793 (1998).
100. Yun, J. *et al.* Cdk2-dependent Phosphorylation of the NF-Y Transcription Factor and Its Involvement in the p53-p21 Signaling Pathway. *J. Biol. Chem.* **278**, 36966–36972 (2003).
101. Kitzmann, M. *et al.* cdk1- and cdk2-Mediated Phosphorylation of MyoD Ser200 in Growing C2 Myoblasts: Role in Modulating MyoD Half-Life and Myogenic Activity. *Mol. Cell. Biol.* **19**, 3167–3176 (1999).
102. Thiel, D. A. *et al.* Cell Cycle-Regulated Phosphorylation of p21-Activated Kinase 1. *Curr. Biol.* **12**, 1227–1232 (2002).
103. Li, M., Stefansson, B., Wang, W., Schaefer, E. M. & Brautigan, D. L. Phosphorylation of the Pro-X-Thr-Pro site in phosphatase inhibitor-2 by cyclin-dependent protein kinase during M-phase of the cell cycle. *Cell. Signal.* **18**, 1318–1326 (2006).
104. Jain, S. *et al.* ATPase-Modulated Stress Granules Contain a Diverse Proteome and Substructure. *Cell* **164**, 487–498 (2016).
105. Fong, K. *et al.* Whole-genome screening identifies proteins localized to distinct nuclear bodies. *J. Cell Biol.* **203**, 149–164 (2013).

106. Dopie, J., Sweredoski, M. J., Moradian, A. & Belmont, A. S. Tyramide signal amplification mass spectrometry (TSA-MS) ratio identifies nuclear speckle proteins. *J. Cell Biol.* **219**, (2020).
107. Liu, J. *et al.* Functional proteomic analysis of promyelocytic leukaemia nuclear bodies in irradiation-induced MCF-7 cells. *J. Biochem.* **148**, 659–667 (2010).
108. Hubstenberger, A. *et al.* P-Body Purification Reveals the Condensation of Repressed mRNA Regulons. *Mol. Cell* **68**, 144-157.e5 (2017).
109. Stenström, L. *et al.* Mapping the nucleolar proteome reveals a spatiotemporal organization related to intrinsic protein disorder. *Mol. Syst. Biol.* **16**, e9469 (2020).
110. Tafforeau, L. *et al.* The complexity of human ribosome biogenesis revealed by systematic nucleolar screening of Pre-rRNA processing factors. *Mol. Cell* **51**, 539–51 (2013).
111. Lin, D. H. & Hoelz, A. The Structure of the Nuclear Pore Complex (An Update). *Annu. Rev. Biochem.* **88**, 725–783 (2019).
112. Machyna, M., Heyn, P. & Neugebauer, K. M. Cajal bodies: where form meets function. *WIREs RNA* **4**, 17–34 (2013).
113. Quevedo, M. *et al.* Mediator complex interaction partners organize the transcriptional network that defines neural stem cells. *Nat. Commun.* **10**, 1–15 (2019).
114. Piovesan, D. *et al.* MobiDB: intrinsically disordered proteins in 2021. *Nucleic Acids Res*. doi:10.1093/nar/gkaa1058.
115. Gentleman, R. C. *et al.* Bioconductor: open software development for computational biology and bioinformatics. *Genome Biol.* **5**, 1–16 (2004).
116. Douglass, J. *et al.* Identifying protein kinase target preferences using mass spectrometry. *Am. J. Physiol. Cell Physiol.* **303**, C715–C727 (2012).
117. Jumper, J. *et al.* Highly accurate protein structure prediction with AlphaFold. *Nature* **596**, 583–589 (2021).
118. Mariani, V., Biasini, M., Barbato, A. & Schwede, T. lDDT: a local superposition-free score for comparing protein structures and models using distance difference tests. *Bioinformatics* **29**, 2722–2728 (2013).
119. Varadi, M. *et al.* AlphaFold Protein Structure Database: massively expanding the structural coverage of protein-sequence space with high-accuracy models. *Nucleic Acids Res.* **50**, D439–D444 (2022).
120. Akdel, M. *et al.* A structural biology community assessment of AlphaFold 2 applications. 2021.09.26.461876 Preprint at https://doi.org/10.1101/2021.09.26.461876 (2021).

121. Mészáros, B., Erdos, G. & Dosztányi, Z. IUPred2A: context-dependent prediction of protein disorder as a function of redox state and protein binding. *Nucleic Acids Res.* **46**, W329–W337 (2018).
122. Erdős, G. & Dosztányi, Z. Analyzing Protein Disorder with IUPred2A. *Curr. Protoc. Bioinformatics* **70**, e99 (2020).
123. Dignon, G. L., Zheng, W., Kim, Y. C., Best, R. B. & Mittal, J. Sequence determinants of protein phase behavior from a coarse-grained model. *PLoS Comp. Biol.* **14**, e1005941 (2018).
124. Regy, R. M., Thompson, J., Kim, Y. C. & Mittal, J. Improved coarse-grained model for studying sequence dependent phase separation of disordered proteins. *Protein Sci.* **30**, 1371–1379 (2021).
125. Abraham, M. J. *et al.* GROMACS: High performance molecular simulations through multi-level parallelism from laptops to supercomputers. *SoftwareX* **1–2**, 19–25 (2015).
126. Feldman, H. J. & Hogue, C. W. A fast method to sample real protein conformational space. *Proteins* **39**, 112–131 (2000).
127. Feldman, H. J. & Hogue, C. W. V. Probabilistic sampling of protein conformations: new hope for brute force? *Proteins* **46**, 8–23 (2002).
128. Pettersen, E. F. *et al.* UCSF Chimera--a visualization system for exploratory research and analysis. *J. Comput. Chem.* **25**, 1605–1612 (2004).
129. Case, D. A. *et al.* The Amber biomolecular simulation programs. *J. Comput. Chem.* **26**, 1668–1688 (2005).
130. Dignon, G. L., Zheng, W., Best, R. B., Kim, Y. C. & Mittal, J. Relation between single-molecule properties and phase behavior of intrinsically disordered proteins. *Proc. Natl. Acad. Sci. U. S. A.* **115**, 9929–9934 (2018).
131. Studier, F. W. Protein production by auto-induction in high density shaking cultures. *Protein Expr. Purif.* **41**, 207–234 (2005).
132. Vranken, W. F. *et al.* The CCPN data model for NMR spectroscopy: development of a software pipeline. *Proteins* **59**, 687–696 (2005).
133. Markley, J. L. *et al.* Recommendations for the presentation of NMR structures of proteins and nucleic acids. *J. Mol. Biol.* **280**, 933–952 (1998).